Self-archived version of the article published in Physical Sciences Reviews:
N. Cancilla, L. Gurreri, M. Ciofalo, A. Cipollina, A. Tamburini, G. Micale
Mathematical modelling of hollow-fiber haemodialysis modules, Physical Sciences Reviews, vol. 10, no. 1-2, 2025, pp.11-50. https://doi.org/10.1515/psr-2024-0062

Mathematical modelling of hollow-fiber haemodialysis modules

N. Cancilla[1], L. Gurreri[2], M. Ciofalo[1], A. Cipollina[1], A. Tamburini[1], G. Micale[1]

[1]Dipartimento di Ingegneria, Università degli Studi di Palermo,
Viale delle Scienze Ed. 6, 90128 Palermo, Italy
e-mail: nunzio.cancilla@unipa.it; michele.ciofalo@unipa.it; andrea.cipollina@unipa.it; alessandro.tamburini@unipa.it; giorgiod.maria.micale@unipa.it.

[2]Dipartimento di Ingegneria Elettrica, Elettronica e Informatica, Università di Catania,
Viale Andrea Doria 6 Ed. 3, 95125 Catania, Italy
e-mail: luigi.gurreri@unict.it

Abstract

This chapter provides an overview of the principles and modelling of membrane-based modules for haemodialysis, the most common renal replacement therapy. Following an introduction on the structure, function and diseases of the kidney, the technological evolution of membranes for blood purification is outlined and the main transport mechanisms involved are described, making a distinction between pure haemodialysis, haemodiafiltration and haemofiltration. The main performance figures of a hollow-fiber module are introduced and their dependence on the parameters that characterize the device is illustrated. A multi-scale modelling approach is then presented, in which preliminary single-fiber CFD simulations are used to derive the hydraulic permeability of a fiber bundle and the relevant mass transfer coefficients as functions of the local velocities. The predicted correlations are then fed to a module-scale model, in which blood and dialysate compartments are simulated as interpenetrated porous media while appropriate source terms account for the exchange of solutes and water between the two fluids. The model predictions are three-dimensional flow and concentration distributions, from which, in particular, performance figures such as clearance and ultrafiltration flow rate can be extracted as functions of the module geometrical and physical characteristics. Validation tests are also presented and the results of a parametrical sensitivity assessment are discussed.

Keywords: Renal replacement treatment; Haemodialysis; Porous media; Permeability; Mass transfer; Computational Fluid Dynamics; Hollow-fiber membrane

1. Introduction

Although this chapter is dedicated to the mathematical modelling of renal replacement devices (notably haemodialysis modules), a brief introduction on the healthy kidney and its pathologies can be useful to identify the functions that a replacement treatment must reproduce and the main causes that may make it necessary.

1.1 Structure and function of the kidney

The function of the kidney is to filter the blood, allowing free flux of water and small solutes (salts and potentially toxic molecules such as urea), but sieving macromolecules and retaining large plasma proteins (e.g. albumin) and all the cellular components of blood.

Most of these functions are accomplished in the kidney glomerulus [1]. As illustrated in **Figure 1**, it is a tuft of anastomosing capillaries surrounded by a spheroidal enclosure (Bowman's capsule). The blood enters the glomerulus through an afferent arteriole, which branches into the capillary tuft. The glomerular filtrate is forced out of the capillaries by the hydrostatic pressure of the blood, is collected in Bowman's capsule and is then funnelled into the renal tubule (whose proximal portion is visible in the bottom part of **Figure 1**), where re-absorption of most of the fluid and small ionic solutes (salts) occurs.

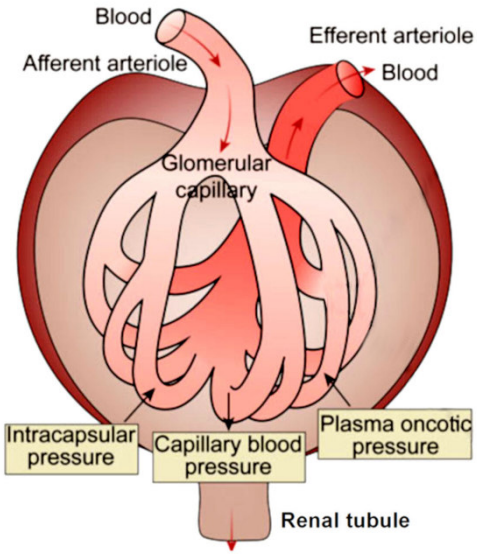

Fig. 1: The kidney glomerulus. Reproduced (adapted) from Huang et al. [2].

The typical (relative) hydrostatic pressure in Bowman's capsule is ~20 mmHg, while that inside the glomerular capillaries is ~50 mmHg [3]; taking the adverse osmotic pressure gradient

into account, the driving pressure difference (ultrafiltration pressure) is of the order of 10 mmHg, or ~1330 Pa [4].

A section of the glomerular capillary wall (GCW) is shown schematically in **Figure 2**. It includes, from top to bottom (luminal to capsule sides):

- the endothelial layer, widely and irregularly fenestrated. **Fenestrae** have diameters of 50 to 100 nm and, unlike in other fenestrated capillaries, are not closed by true diaphragms;
- the glomerular basement membrane (GBM), or basal lamina;
- the foot processes (podocytes) of the epithelial cells, which face the urinary spaces (Bowman capsule) and are separated by gaps of ~25 nm (epithelial slits).

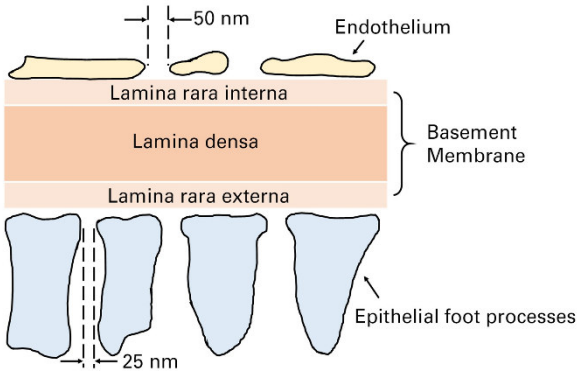

Fig. 2: Cross section of the glomerular capillary wall (GCW).

The GBM [5, 6] is the main structure where renal filtration takes place. It is composed of three layers, from luminal to capsule side: a **lamina rara interna** (LRI); a **lamina densa** (LD); and a **lamina rara externa** (LRE). In most mammals, the **lamina densa** is ~80 – 100 nm thick, while the **laminae rarae** are thinner (20 – 40 nm). The three **laminae** are all of fibrous nature, but differ in ultrastructure and chemical composition:

- the **laminae rarae** are networks of heparan sulphate proteoglycans and attachment glycoproteins including entactin, laminin and fibronectin, which anchor the endothelial or epithelial cells to the GBM and are continuous with their glycocalyx [7, 8];
- the **lamina densa** is a more compact fibrillar meshwork layer mainly containing type IV collagen and sialic acid; individual **fibrillae** are ~3 nm thick.

Several reviews of glomerular filtration and its molecular, structural and functional determinants have been presented [9, 10]. Generally speaking, the GBM has size–, shape– and charge–selective properties.

- In regard to size selectivity, it has been known for a long time that large macromolecules do not have access to the urine [11]. Chang et al. [12], using dextran, showed that neutral molecules with diameters less or equal to that of inulin (2.8 nm) have a fractional clearance of 1; as size increases, the fractional clearance decreases following a sigmoidal curve and is ~0.1 for albumin (~7 nm diameter). The clearance for neutral molecules is practically zero for diameters above 8–9 nm in all animal species.
- In regard to charge selectivity, it is well known that the glomerular barrier is more permeable to cationic macromolecules, as a consequence of possessing fixed anionic charges [13–15].
- Also the shape and flexibility of molecular species can influence their transmission through the glomerular barrier [16]. For example, for the same molecular diameter, Ficoll – an uncharged, highly coiled polymer – is arrested in the glomerular capillary wall to a greater extent than the less coiled neutral Dextran.

Bohrer et al. [17] compared clearance curves obtained in normal rats for neutral Dextran, anionic Dextran Sulfate and cationic DEAE (Diethylaminoethyl) Dextran, and showed that clearance was highest for the cationic species, lowest for the anionic one and intermediate for neutral Dextran.

The main size– and charge–selective "sieve" in the GBM is the network of proteoglycans, particularly in the **lamina rara interna**. The GAG moieties of heparan sulphate proteoglycans are among the most highly negative (anionic) biomolecules, and their presence in the **laminae rarae**, where they are arranged in lattice-like regular arrays, is crucial to the size- and charge-selectivity of the glomerular capillary wall.

An additional function of the sulphated proteoglycans is to protect the glomerular capillary wall from being "clogged" by plasma macromolecules [18]. Work with synthetic membranes constructed from similar sulphated polymers [19] has shown that the sulphate groups are highly hydrophilic and thus do not form hydrogen bonds with the molecules present in the solution to be filtered; a similar mechanism may be operating in natural, biological membranes.

1.2 Kidney diseases and malfunction

Kidney diseases affect today over 850 million people in the world [20]. Two million people worldwide suffer from End–Stage Renal Disease (ESRD), and the growth rate of patients is 5–7% per year [21]. These figures are expected to increase due to the recent COVID–19 pandemic:

according to the US National Institutes of Health, in 2020 around 5% of the COVID–19 patients were having acute kidney injury requiring renal replacement therapy [22].

Renal diseases can be divided into two main groups:

- Acute Kidney Injury (AKI) refers to a kidney malfunction characterized by a rapid deterioration of its functions. AKI is usually reversible but an incomplete recovery can lead to progress to the later stages of the disease.
- Chronic Kidney Disease (CKD) refers to a sustained kidney damage indicated by the presence of structural or functional abnormalities. There are five levels of CKD, the last of which requires treatments such as dialysis or kidney transplantation as the only option.

Renal pathophysiology in general is treated, for example, by Leaf et al. [23]. Proteinuria, the anomalous increase of the excretion of proteins and other macromolecules in the urine, occurs whenever a pathologic or toxic condition alters the permselectivity of the renal glomerulus [24].

In the same paper cited shortly above [17], Bohrer et al. showed that the charge selectivity exhibited by clearance curves for normal rats was lost when rats affected by Nephrotoxic Serum Nephritis (NSN) were tested. Similar results are obtained for other kidney diseases such as Aminonucleoside Nephrosis, or ANN [25, 26].

Puromycin, the drug used to induce ANN, causes changes in the structure of the glomerular wall similar to those seen clinically in patients with the so called Minimal Change Nephrotic Syndrome, or MCNS [27]. These effects are also similar to those produced by Neuraminidase [18] and can be attributed to a partial disruption of the glycoprotein matrix in the epithelial glycocalix and in the **lamina rara externa** of the glomerular basement membrane. Robson et al. [28] and Bohrer et al. [29] observed that ANN or the related MCNS cause a reduced clearance of neutral molecules, but increase the clearance of anionic species (e.g. albumin). This is the effect expected if a partial disruption of anionic sites leads to macromolecular "clogging" of the GBM, thus reducing charge selectivity but possibly increasing the resistance to uncharged, large macromolecules.

Charge selectivity remains basically unchanged in other syndromes, e.g. Autologus Immune Complex Nephritis and Adriamycin-Induced Proteinuria [30].

Barnes and Venkatachalam [31] studied the influence of polyanion neutralisation by the synthetic polycation Polyethyleneimine (PEI) or by Platelet Factor 4 (PF4), which also behaves as a cationic macromolecule, on the glomerular permeability to native (anionic) and cationised ferritin in the rat. Neutralisation resulted in the increase (by a factor of 100 or more) of the

clearance of native (anionic) ferritin, but affected to a much lesser extent that of cationised ferritin, confirming the electrostatic nature of the main glomerular resistance to anionic molecules. However, the residual influence of neutralisation on the penetration of cationic ferritin was interpreted as a sign that PEI somehow perturbed also the structural integrity (size selectivity) of the barrier; the simple neutralisation of polyanionic sites, with no change in the architecture of the glomerular basement membrane and its annexes, should lead to a reduction of the clearance of cationic probes, not to its (however moderate) increase. Platelet factor 4 was shown to bind avidly to glomerular polyanions, suggesting that endogenous cationic molecules released from platelets during immune glomerular disease may alter glomerular permeability and favour the precipitation of immune complexes.

Seiler et al. [32] observed that perfusion of rat kidneys with the polycation protamine sulphate produced a fusion of foot processes of the epithelium of glomerular capillaries similar to that observed in experimental nephrotic syndromes induced by puromycin or neurominidase (see above), but reversible by perfusion with the strong polyanion heparin. This suggests that neutralisation, and not removal, of glomerular polyanions is implied here. It also suggests that one of the consequences of nephrotic diseases and of polycation administration may be the loss of the repulsive forces between epithelial foot processes which maintain their normal architecture, thus leading to their disorganisation and fusion.

In regard to the influence of pressure and flow on the permeability of glomerular capillaries, Barnes and Venkatachalam [31] reported that changes in the kidney perfusion pressure had no effect on the permeability to ferritin. However, data from Chang et al. [12, 33] indicate a significant influence of glomerular capillary pressure and trans-capillary flow on dextran clearance profiles.

The effect of angiotensin has been studied, for example, by Eisenbach et al. [34], while the effect of vasodilators was investigated by Baylis et al. [35]. As expected, renal vasoconstriction reduces renal perfusion and glomerular filtration rate, whereas vasodilators like calcium antagonists reverse renal vasoconstriction and improve renal perfusion.

2. Membrane–based Renal Replacement Treatments (RRT)

Most Renal Replacement Treatments (RRT) are extracorporeal blood filtering procedures which typically make use of hollow fiber membrane modules. An alternative is Peritoneal Dialysis, a treatment which uses the body's own peritoneal membrane, lining the abdominal cavity and highly vascularized, to assist or replace the kidneys' functions. Waste solutes and

180 excess water move through diffusion and ultrafiltration from the blood vessels into a fluid
181 (dialysate) filling the peritoneal cavity. After a set amount of time, the dialysate with the filtered
182 waste is let to flow out of the abdomen and is disposed of.
183
184 *2.1 Technological evolution of membrane modules for haemodialysis*
185 The basic functions of a haemodialysis membrane are the following:
186 • separating waste solutes and excess fluid from the patient's blood;
187 • restoring the electrolyte balance in the body;
188 • achieving the lowest possible activation of blood components at the membrane surface
189 (haemocompatibility);
190 • possessing adequate thermal, mechanical and chemical stability (properties must remain
191 unaltered during the manufacturing steps and the sterilization).
192 To this purpose, some characteristics are required. First, a thin and hydrophilic separation
193 layer is necessary to provide high transmembrane flux in conjunction with low protein
194 absorption. Second, the membrane should have a narrow pore size distribution to attain the right
195 selectivity; the maximum pore size should be such that the loss of albumin is prevented. Third,
196 a high overall porosity of the membrane wall is desired to achieve high hydraulic permeability.
197 Finally, also the choice of the material is important for the characterization of the separation
198 properties and the biocompatibility of the membrane.
199 Haemodialysis membranes have historically been classified into three categories according
200 to the material composition of the polymers: unmodified cellulosic membranes, modified
201 cellulosic membranes, and synthetic membranes [36–40].
202 Cellulosic membranes are highly hydrophilic due to the presence of hydroxyl groups, and
203 form a hydrogel when absorbing water. Intensively used in the past, they have now been
204 dismissed for two main reasons. One is their high permeability to water, which induces the
205 swelling phenomenon enhancing water flow but reducing selectivity and, thus, compromising
206 the patient's health. Another reason is that the hydroxyl groups cause biocompatibility problems
207 [41–43]. Modified cellulose derivatives such as cellulose diacetate, cellulose triacetate, and
208 diethylaminoethyl–substituted cellulose were developed with the aim of improving
209 biocompatibility. Most cellulose membranes (modified or not) have a thickness of 5–11 μm and
210 a surface of 0.8–2.5 m^2.
211 Synthetic membranes are now those most used for dialysis treatments. Their thickness is
212 20–50 μm, larger than in cellulosic membranes [44]. They include sulphonated

polyacrylonitrile and polymethylmethacrylate membranes [45], which are structurally symmetric (like the cellulosic membranes) and possess a uniform homogenous structure throughout the entire membrane wall. However, most synthetic membranes (i.e., polysulfone, polyethersulfone, polyamide, polyacrylonitrile polyvinylchloride copolymer) are asymmetric [36]. They are characterized by a thin selective skin layer of ~1 μm at the membrane–blood interface, where the actual separation process takes place, and by a thick spongy bulk providing mechanical strength. For high-flux synthetic membranes, the average pore size of the skin layer is usually in the range of 3–5 nm, while the pore size in the spongy layer can be greater than 10 nm. For low-flux synthetic membranes, the inner skin layer mean pore size is ~1 nm [46]. Polyethersulfone (PES) membranes are typically additivated using polyvinylpyrrolidone (PVP) to make the final hollow fibers sufficiently hydrophilic. PVP increases the viscosity of the polymer solution and improves the hollow fiber properties during manufacturing [47]. This blend is higher in porosity, with well-interconnected pores and a very small macrovoid formation. PVP is mainly located at the surface of the pores in the skin thanks to its hydrophilicity [48].

Another criterion often used to categorize dialysis membranes is their hydraulic permeability. The clinical parameter used is the ultrafiltration coefficient, K_{UF}, typically expressed in mL/(m^2 h mmHg) (multiply K_{UF} by ~$2 \cdot 10^{-12}$ to express it in SI units, i.e. m/(s Pa)). K_{UF} is empirically measured from *in vitro* experiments by membrane manufacturers as the ratio between the ultrafiltration flow rate (Q_{UF}) and the transmembrane pressure. Membranes having K_{UF} lower than 10 mL/(m^2 h mmHg) are classified as low–flux ones, those with K_{UF} higher than 25 mL/(m^2 h mmHg) as high–flux ones and those with $10 \leq K_{UF} \leq 25$ mL/(m^2 h mmHg) as medium-flux ones [44, 49].

2.2 Transport mechanisms of solute removal: haemodialysis, haemofiltration, haemodiafiltration

Haemodialysis is a membrane-based technique where solute removal primarily occurs through diffusion across the membrane [50]. It involves two fluids: the blood, containing toxic substances, and a rinsing solution called dialysate, separated by the membrane. The dialysate is prepared by diluting a concentrated aqueous solution of electrolytes and sometimes glucose with ultrapure water. It contains sodium, chloride and magnesium ions at concentrations equivalent to those found in normal plasma. To preserve the pH balance of the solution, bicarbonate or acetate may also be added [51, 52].

The core of the process is the semi-permeable membrane [44]. A membrane is characterized by its cutoff, defined as the lowest molecular weight of a solute 90% of which is retained by the membrane. In haemodialysis, the cutoff can vary from one membrane to another but, usually, it is less than 50,000 Da. This value is slightly lower than the molecular weight of albumin (~69,000 Da), an important blood protein that, as already mentioned, must not be removed during the haemodialysis process as it regulates some biological functions such as the maintenance of osmotic pressure and the transport of various hormones.

Most devices used in haemodialysis therapies (haemodialyzers) are cylindrical modules, typically 2–5 cm in diameter and 15–25 cm in length. The housing is typically made from a transparent polymeric material, such as polycarbonate or polypropylene, and encompasses a bundle of several thousand (approximately 8,000–16,000) hollow fibers. The bundle has defined characteristics, including the fiber spatial arrangement and packing density. The module (**Fig. 3**) is also equipped with inlet and outlet ports for the two fluids [53, 54].

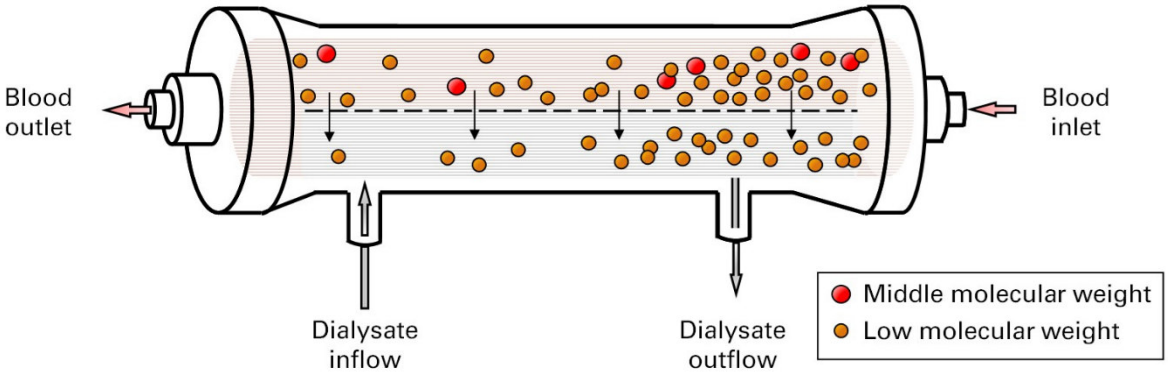

Fig. 3: Schematic of the diffusion mechanism in a haemodialysis module.

Within the hollow fibers, blood flows through the lumen, while the dialysate flows outside the fiber bundle in a counter-current arrangement. The main driving force for solute mass transfer is the concentration gradient between the two compartments. Solutes are transferred from the blood to the dialysate through the membrane wall via diffusive–convective mass transfer, driven by both concentration gradients and pressure differences between the blood and dialysate [54].

In principle, haemodialysis can be divided into **standard** haemodialysis and **high-flux** haemodialysis, according to whether low-flux or high-flux membranes are employed. In modules using low-flux membranes, the contribution of ultrafiltration is negligible, while it is significant in high-flux modules, since they use membranes of higher hydraulic permeability.

Diffusive mass transfer mainly occurs according to the molecular weight of the solute to be removed. Solutes in the blood can be classified into three main categories, according to their molecular weight (**Tab. 1**), as defined by the European Uremic Toxin Work (EUTox).

Tab. 1: Molecular weight of the main solutes in human blood.

Solute	Molecular weight (Da)
Albumin	69,000
Erythropoietin (EPO)	34,000
Myoglobin	17,000
Beta–2 microglobulin	11,800
Endotoxin fragments	1,000-15,000
Inulin	5,200
Vancomycin	1,448
B_{12}Vitamin	1,355
Aluminum/Desferoaxamine Complex	700
Glucose	180
Uric acid	168
Creatinine	113
Phosphate	80
Urea	60
Potassium	35
Phosphorus	31
Sodium	23

Molecules with a molecular weight less than 500 Da (e.g. urea or creatinine) are referred to as low-molecular weight solutes [55, 56]; they are removed from the blood mainly by diffusion. In particular, urea is often used as the main marker for the success and control of the dialytic treatments. Medium-molecular weight solutes are in the range between 500 Da and 15,000 Da; they include various proteins (e.g., Beta–2 microglobulin). Solutes of this category are mainly removed by convective mass transport and the influence of convection on total removal rises with rising molecular size [57]. Molecules with molecular weight higher than 15,000 Da (e.g. Myoglobin and EPO) are considered high-molecular weight solutes.

Significant diffusive removal can only occur if the membrane cut–off is greater than the size of the solute. In **standard haemodialysis** this threshold is very low, so that medium and high molecular weight solutes are not removed; in **high-flux** haemodialysis, the internal ultrafiltration caused by a transmembrane pressure gradient is not negligible [58, 59], so that convective mass transfer gives an important contribution, although it is smaller than in haemofiltration or haemodiafiltration.

In regard to flow rates, typical operating conditions are in the range 200–500 mL/min for the blood and 500–800 mL/min for the dialysate. The blood flow rate is limited by the vascular

entry; regarding dialysate, the flow rate can potentially be enhanced, but clinical practice has shown that the upper limit is ~twice the blood flow rate. This condition is preferred in order to maximize the diffusive transport. If the blood flow rate is to be increased, also the dialysate one must be enhanced in order to keep this ratio constant.

Haemofiltration is a blood treatment in which a large amount of ultrafiltration is realized, through a high hydraulic pressure applied on the membrane, characterized by a high hydraulic permeability, without the use of a dialysis bath (**Fig. 4**). Solute removal occurs only by convection, up to the membrane cutoff. This technique removes solutes with a molecular weight higher than those of the toxins rejected by **standard** haemodialysis treatments.

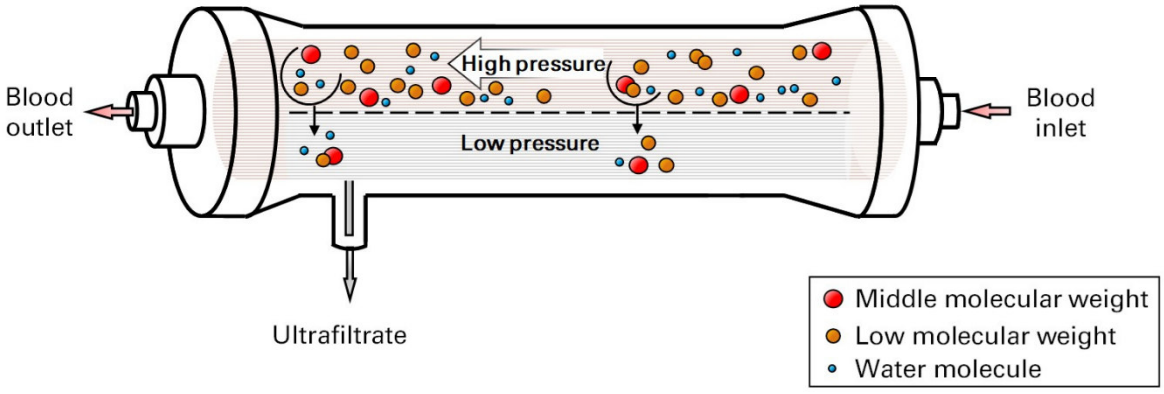

Fig. 4: Schematic of the ultrafiltration mechanism in a haemofiltration module.

In haemofiltration, the plasmatic water subtracted by ultrafiltration is replaced by reinfusion. It is carried out with sterile and non-pyrogenic liquids with a controlled composition that allows the reconstitution of the blood volume. Reinfusion can take place before or after the blood purification in the module (**pre– or post–dilution)**. Pre–dilution allows to operate in better blood rheological conditions, improving the performance of the module in the long term. In fact, the reinfusion leads to decreased values of haematocrit and viscosity: possible problems, such as **clotting** or coagulation inside the membranes, are thus limited. The disadvantage is that, by increasing the volume of the plasma before the treatment, the clearance of each solute is obviously lower. Conversely, post–dilution increases the risk of incurring in blood **clotting**, but allows for higher clearance values to be achieved. With haemofiltration, it is very difficult to obtain clearances for low molecular weight solutes (e.g., urea and creatinine) comparable to those achieved by haemodialysis. Therefore, on one hand, haemofiltration guarantees better performance regarding medium–high molecular weight solutes while, on the other hand, it is

characterized by a slower removal of the smaller solutes, actually reversing the problem of standard haemodialysis.

Haemodiafiltration is a diffusive and convective treatment which combines the advantages of haemofiltration with a good purification of small molecules allowed by the dialysate flow rate. Many researchers have studied the simultaneous effect of diffusion and convection on mass transfer [60-66]. The process consists of obtaining a certain amount of ultrafiltration, one part of which is reintegrated by infusion of suitable liquid (haemofiltration), and the other part is simultaneously passed through the module (haemodialysis). Also for haemodiafiltration, reinfusion can take place both before and after the module, although **post–dilution** is more common. The pros and cons of **pre–** and **post–dilution** are the same discussed above for haemofiltration. The two approaches are schematically illustrated in **Figure 5**.

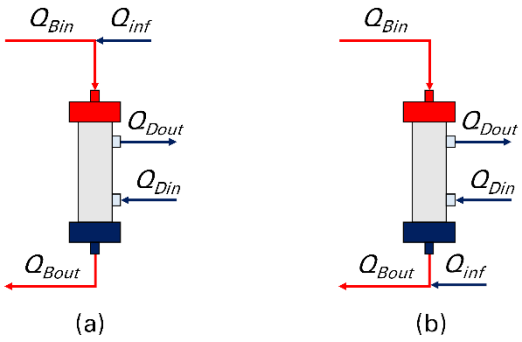

Fig. 5: Schematic representation of modules for haemodiafiltration treatment: (a) reinfusion in pre–dilution and (b) reinfusion in post–dilution.

There is a negative interference between diffusion and convection, so that, as the ultrafiltration flow rate increases, the convective effect also increases to the detriment of the diffusive one [67]. Thus, the removal of different molecular weight solutes can be selectively tuned, favouring diffusion or convection, by modifying Q_{UF}. A fairly common ultrafiltration flow rate for haemodiafiltration is Q_{UF} = 90 mL/min.

The introduction of the convective transport mechanism results in the appearance of **backfiltration**. It occurs when the transmembrane pressure gradient at some location in the module becomes negative: the dialysate pressure, together with the oncotic pressure, exceeds the pressure of the blood compartment. This allows the passage of water and solutes from dialysate to blood [68]. Rangel et al. [69] extensively reviewed various aspects of backfiltration, in particular the effect of increasing or diminishing this phenomenon in the different

haemodialysis techniques, investigating the possibility of exploiting backfiltration to enhance the convective clearance of middle and large solutes.

Extracorporeal blood treatments for End–Stage Renal Disease are summarized in **Table 2**, divided according to the transport phenomena involved.

Tab. 2: Extracorporeal blood treatment for End–Stage Renal Disease.

Treatment	Diffusive solute transport	Convective solute transport
Standard haemodialysis	high	minimal
High flux haemodialysis	high	medium
Haemodiafiltration	high	high–very high
Haemofiltration	none	very high

3. Performance figures and quantities affecting them

For any given solute to be removed from the blood, the main performance figure characterizing a haemodiafiltration module is the clearance *CL*, commonly defined as the ratio of solute mass removal rate and solute concentration in the inflowing blood:

$$CL = \frac{Q_{Bin} C_{Bin} - Q_{Bout} C_{Bout}}{C_{Bin}} \tag{1}$$

where Q_{Bin} and Q_{Bout} are the blood flow rates at the module inlet and outlet, respectively, while C_{Bin} and C_{Bou} are the inlet and outlet bulk solute concentrations in the blood. Clearance can be interpreted as the blood volume which should be completely purified in the time unit to yield a given solute removal rate. For urea (MW = 60 Da), typical clearance values range from 80% to 90% of the inlet blood flow rate Q_{Bin} (e.g. from 240 to 270 mL/min for Q_{Bin} = 300 mL/min). Clearance values are markedly lower for larger solutes, e.g. from 50% to 60% of Q_{Bin} for B12 vitamin (MW = 1355 Da).

A performance figure which characterizes the nature of the haemodiafiltration process occurring in the module is the ultrafiltration flow rate $Q_{UF} = Q_{Bin} - Q_{Bout}$, which is nil in pure haemodialysis and increases as the relative importance of ultrafiltration increases.

Eq. (1) can be re-formulated so as to evidence the contribution of Q_{UF}:

$$CL = \frac{C_{Bin} - C_{Bout}}{C_{Bin}} Q_{Bin} + \frac{C_{Bout}}{C_{Bin}} Q_{UF} \tag{2}$$

Performance figures depend on the physical, geometric and operating parameters characterizing the module, and the main object of a parametrical study aimed at improving or optimizing the module performance will be their prediction as functions of said parameters.

Assuming that the cylindrical, counter-flow configuration has been adopted, a possible set of such parameters includes the following 11 independent quantities:

- Fiber inner diameter, d_i
- Fiber outer diameter, d
- Blood inlet flow rate, Q_{Bin}
- Dialysate inlet flow rate, Q_{Din}
- Relative bloodoutlet pressure, p_{Bout}
- Module aspect ratio (active length to inner diameter), L/D
- Bundle porosity, ε
- Membrane surface area, S
- Membrane diffusive permeability, k_M
- Membrane hydraulic permeability, L_p
- Solute rejection coefficient σ

Also the geometry of the headers may play some role, by affecting to some extent the flow distribution in the module. Note that k_M and σ are solute-dependent, while all other parameters are the same for all solutes. Note also that, if blood and dialysate are regarded as incompressible fluids, their absolute pressure is irrelevant and thus the outlet pressure of the dialysate can be arbitrarily assumed as zero (i.e., all pressures will be interpreted as relative to it).

Other quantities characterizing the module can be derived from the above ones. For example, the following relations exist between bundle porosity ε, number of fibers N, fiber outer diameter d, and module inner diameter D and active length L:

$$1-\varepsilon = \frac{N\pi d^2/4}{\pi D^2/4} \tag{3}$$

$$S = N\pi dL \tag{4}$$

(assuming the fibers to be straight and parallel), from which explicit expressions are obtained for the module inner diameter D and length L:

$$D = \left[\frac{Sd}{\pi(1-\varepsilon)(L/D)}\right]^{1/3} \tag{5}$$

$$L = \left[\frac{Sd}{\pi(1-\varepsilon)}\right]^{1/3} (L/D)^{2/3} \tag{6}$$

4. Small–scale (unit cell) modelling of the haemodialysis process

4.1 Regular lattices: single–fiber models

While the modelling of the lumen side flow is quite simple, the study of the shell side flow is more complex. A simplified way of modelling these devices is to consider a regular (square or hexagonal) uniform fiber lattice. A set of simplifying assumptions can be made:

- The flow is steady, fully developed and laminar.
- The fibers are cylindrical, straight and oriented parallel to the longitudinal z axis.
- All fibers have the same diameter.
- The flow and concentration structures strictly follow the spatial periodicity of the fiber arrangement.
- The fluid's physical properties, including density, dynamic viscosity and scalar diffusivity, are constant.
- Gravity is neglected, as its only effect in a constant-density fluid is to induce vertical static pressure stratification, which does not impact the flow field.

The first four assumptions allow the adoption of the unit cell approach [70]: the computational domain is two-dimensional and consists of a repetitive periodic unit of the bundle, including a single fiber.

The following sections mainly cover the case of fibers bundle arranged in a regular hexagonal lattice, since it represents the most realistic case with respect to a real bundle. Similar modelling strategies are adopted by several researchers [71-74] by assuming the fibers arranged in a square lattice. The different CFD modelling tools have been developed by finite-volume (FV) or finite-element (FE) methods. Several studies adopted commercial software, for example, Ansys® CFX® [75] or Fluent® [76] (FV codes), or COMSOL Multiphysics® [77, 78] (FE code). The open-source FV OpenFOAM code [79] is another option.

4.1.1 Definitions for flow and mass transfer characterization

The bundle porosity ε was defined as:

$$\varepsilon = \frac{A}{A_{tot}} \tag{7}$$

in which A_{tot} is the total area while A is the fluid area in a generic cross section.

The definition of Reynolds number along a generic direction s of unit vector $\vec{\sigma}$ is:

$$\mathrm{Re}_s = \frac{\rho \langle u_s \rangle d_h}{\mu} \tag{8}$$

where ρ is density, μ is dynamic viscosity, $\langle u_s \rangle$ is the average of the superficial velocity component $u_s = \vec{u} \cdot \vec{\sigma}\varepsilon$ along the same direction and $d_h = 4V/S$ is the hydraulic diameter, V being the volume of fluid and S the wet surface in the computational domain (in a 2-D domain, d_h can be expressed as $4A/(\pi d)$). The Darcy friction coefficient f_s relative to the generic direction s is defined:

$$f_s = \frac{\left|\mathrm{d}p/\mathrm{d}s\right| 2d_h}{\rho \langle u_s \rangle^2} \tag{9}$$

in which p is pressure. The Darcy permeability K_s relative to the generic direction s is:

$$K_s = \frac{\mu \langle u_s \rangle}{\left|\mathrm{d}p/\mathrm{d}s\right|} \tag{10}$$

In the literature, the permeability is often expressed in dimensionless form, e.g. as K_s/d^2 (d being the outer fiber diameter) or by introducing the so called Kozeny "constant" k_K:

$$k_K = \frac{\varepsilon^3}{(1-\varepsilon)^2} \frac{1}{\Sigma^2 K_s} \tag{11}$$

where Σ is the specific surface of the medium particles (for cylinders, $\Sigma = 4/d$). Eq. (11) is usually adopted under the assumption of an isotropic permeability, so that the direction subscript "s" can be omitted from K.

In regard to mass transfer, the average shell-side mass transport coefficient k_D is:

$$k_D = \frac{\overline{J}}{\overline{C}_w - C_b} \tag{12}$$

in which $\overline{J}$ is the wall–averaged molar flux at the wall, $\overline{C}_w$ is the wall–averaged solute concentration at the wall and C_b is the bulk concentration, defined as the mass flow–weighted average of the solute concentration on an arbitrary cross section.

Consistently, the average shell-side Sherwood number is calculated as:

$$\mathrm{Sh} = k_D \frac{d_h}{D} \tag{13}$$

where D is the diffusion coefficient of the solute.

4.1.2 Governing equations and physical properties

For a Newtonian incompressible fluid, the steady-state continuity and momentum equations are:

$$\nabla \cdot \mathbf{u} = 0 \tag{14}$$

$$\rho \mathbf{u} \cdot \nabla \mathbf{u} = -\nabla p + \mu \nabla^2 \mathbf{u} \tag{15}$$

in which $\mathbf{u}$ is the local velocity vector and p is pressure.

The convection-diffusion transport equation governing the concentration field is:

$$\mathbf{u} \cdot \nabla C = D \nabla^2 C \tag{16}$$

C being the solute concentration and D its diffusion coefficient in the fluid.

The fluid was representative of the dialysate in a haemodialysis module. The solution properties were set to ρ=1000 kg/m^3, μ=7.62·10^{-4} Pa·s. For urea, the diffusivity D of the solute in the solution was set to 1.8·10^{-9} m^2/s, so that the Schmidt number, $\mu/(\rho D)$, was 423. For B12-vitamin, D was set to 5·10^{-10} m^2/s so that the Schmidt number was 1524.

4.1.3 Treatment of periodicity for unit cell simulations

In the unit cell approach, in a spatially periodic computational domain, translational periodicity boundary conditions are imposed to all variables on the couples of opposite boundaries under the hypothesis of fully developed flow and concentration fields. However, it is necessary to allow for a streamwise variation of pressure, due to the hydraulic resistance of the medium, and of the bulk concentration, due to solute inflow or outflow through the membrane fiber wall. To this purpose, Eqs. (15) and (16) are treated as follows.

In the fully-developed region of a bundle, the static pressure $p(x, y, z)$ and the concentration $C(x, y, z)$ are decomposed into spatially periodic components $\tilde{p}(x, y, z)$ and $\tilde{C}(x, y, z)$, respectively, whose spatial distribution repeats itself identically in each unit cell, and large-scale components ($-G_p \cdot s$ and $G_c \cdot s$, respectively) linearly varying with a coordinate s:

$$p(x, y, z) = \tilde{p}(x, y, z) - G_p s \tag{17}$$

$$C(x, y, z) = \tilde{C}(x, y, z) + G_c s \tag{18}$$

By substituting p and C as expressed by Eqs. (17) and (18), respectively, in the momentum (Eq. 15) and convection-diffusion (Eq. 16) equations, they become:

$$\rho \mathbf{u} \cdot \nabla \mathbf{u} = -\nabla \tilde{p} + \mu \nabla^2 \mathbf{u} + \mathbf{f} \tag{19}$$

$$\mathbf{u} \cdot \nabla \tilde{C} = D \nabla^2 \tilde{C} + S_C \tag{20}$$

where $\mathbf{f} = G_p \vec{\sigma}$ is a forcing term along the arbitrary direction of unit vector $\vec{\sigma}$, accounting for the non-periodic component of the pressure gradient and compensating for large-scale pressure loss, and $S_C = -G_c u_s$ is a source term compensating the large-scale concentration gradient. From a global balance of solute in the computational domain, G_c can be written as:

$$G_c = \frac{\bar{J} S}{V} \frac{1}{\langle u_s \rangle} \tag{21}$$

in which the quantity $\bar{J}S/V$ is the average value of the source term and $\langle u_s \rangle$ is the volume-averaged velocity component along the s direction.

Apart from numerical approximations, this approach guarantees solute mass conservation: the mean value of the bulk concentration adopted as the initial guess is conserved through the simulation.

4.1.4 Computational domain and boundary conditions

Figure 6 shows the 2-D computational domain (unit cell) for a regular hexagonal lattice with bundle porosity ε=0.5, a typical value for commercial haemodialyzers.

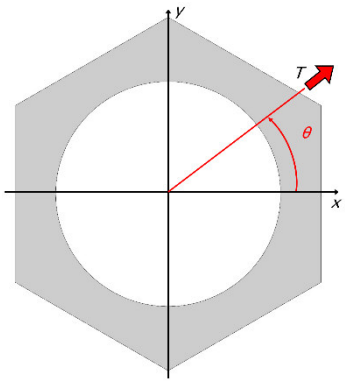

Fig. 6: 2-D cross section of a regular hexagonal lattice with ε=0.5. The cross flow attack angle θ and the mean cross flow direction T in the xy plane are indicated.

As shown in **Figure 6**, the cross-flow attack angle θ is the angle formed in the xy plane by the mean flow direction T with the x-axis. In addition to the longitudinal Reynolds number Re_z, which is calculated using the mean superficial velocity $\langle u_z \rangle$ along the axial direction z, a cross flow Reynolds number Re_T can also be determined. It is defined using the mean superficial velocity $\langle u_T \rangle$, resultant from the mean superficial velocities $\langle u_x \rangle$, $\langle u_y \rangle$

$$\left\langle u_T \right\rangle = \left\langle u_x \right\rangle \cos\theta + \left\langle u_y \right\rangle \sin\theta \tag{22}$$

In regard to hydrodynamics, the cylindrical surfaces representing mass exchange walls were considered as no slip walls.

In regard to mass transfer, a Neumann boundary condition was typically applied, with an arbitrarily assigned value for the mass flux (Sherwood numbers remain unaffected by this choice). The motivation behind this is that the mass flux J crossing the membrane can be described as $\Delta C/(r_l+r_m+r_s)$, in which ΔC is the bulk concentration difference between the lumen and the shell sides, and r_l, r_m and r_s represent the areal resistances of lumen-, membrane- and shell-side, respectively. In haemodialysis, the resistance associated with the membrane is usually the largest between the three resistances in series. Both r_l and r_m can be considered uniform around the circumference of a fiber. On the other hand, the only component showing significant circumferential variations is $r_s = k_D^{-1}$, see Eq. (12), which is only a minor component of the overall resistance. Consequently, J is expected to be almost uniform around a fiber, making Neumann boundary conditions the most representative of the real-world scenarios.

In some simulations, Dirichlet boundary conditions were also evaluated, with the wall concentration set to an arbitrary uniform value (which does not impact k_D). For both boundary conditions, another arbitrary value was assigned to the bulk concentration of the dialysate. As explained in Section 4.1.3, periodicity conditions were applied to all variables at the opposite boundaries of the computational domain.

All runs were conducted in double precision and were stopped once the dimensionless residuals of all variables reduced below 10^{-12}, indicating a very stringent convergence criterion.

A careful grid-independence analysis on the present geometry [75] revealed that both triangular and quadrilateral meshes converge to the same results for increasing number of cells. Convergence is achieved earlier (i.e., for a smaller number of cells) for quadrilateral meshes. ~16,000 cells in the domain's cross sectional plane are sufficient to achieve practically grid-independent results (discrepancy < 1% with respect to the finest grids tested, which included ~128,000 cells in the same plane).

By applying the methodology described in the previous sections, Cancilla et al. [75] developed a single-fiber (unit-cell scale) model. Numerous simulations were carried out, allowing the longitudinal Reynolds number, Re_z, the cross flow Reynolds number, Re_T, and the cross flow attack angle, θ, to vary. For each set of input parameter, the main computational results included the axial and cross-flow Darcy friction coefficients (or Darcy permeabilities) and the average Sherwood number.

4.1.5 Results for axial flow

In axial flow, a pressure gradient was imposed only along the z direction. The Darcy friction coefficient f_z closely follows a Re_z^{-1} behavior, indicating that the permeability K_z, is independent of Re_z. The values of the product $f_z \cdot Re_z$, K_z, Kozeny's "constant" and average Sherwood numbers are reported in **Table 3**. For comparison purposes, results for the square lattice are also given.

Tab. 3: Values of $f_z \cdot Re_z$, permeability K_z, Kozeny's k_K and average Sherwood numbers predicted for regular lattices in axial flow at $\varepsilon = 0.5$. From results in [75].

Geometry	Hexagonal	Square
$f_z \cdot Re_z$ [-]	226	180
$K_z \cdot 10^{10}$ [m^2]	7.60	9.54
Kozeny's k_K [-]	3.57	2.88
Sh, uniform wall mass flux [-]	9.86	5.15
$Sh^{(CW)}$, uniform wall concentration [-]	9.90	5.82

For $\varepsilon = 0.5$, the two lattices provided quite different friction coefficients, with the hexagonal lattice exhibiting a ~23% higher value. A comparison of the CFD predictions in [75] with other results from the literature can be performed using the Kozeny "constant" k_K as defined by Eq. (5), which remains unaffected by the fiber diameter. The results in [75] yielded $k_K \approx 3.57$ and $k_K \approx 2.88$ for the hexagonal and the square lattice, respectively, which are in good agreement with the literature. Happel [72] formulated a simplified analytical model that does not depend on the fiber array. For flow parallel to cylinders at $\varepsilon = 0.5$, the calculated k_K value was 3.67. Sparrow and Loeffler [73] derived analytical solutions for longitudinal laminar flow between cylinders in hexagonal or in square lattices. Their prediction indicated k_K values of ~3.5 and ~2.9, respectively. Skartsis et al. [80] presented both experimental and theoretical results from various authors for axial flow through straight cylinder configurations. This includes the

numerical solution by Larson and Higdon's [81] for square lattices, which estimates k_K to be approximately 2.75 at $\varepsilon = 0.5$.

In regard to mass transfer, the predicted Sherwood number remains unchanged as the longitudinal Reynolds number rises. **Table 3** provides the Sherwood numbers Sh calculated for uniform wall mass flux boundary conditions, as well as the $Sh^{(CW)}$ values calculated for uniform wall concentration boundary conditions. For the hexagonal lattice, the Sherwood number is significantly higher compared to the square one. The Sherwood number values predicted under different boundary conditions are much closer to each other in the case of the hexagonal lattice compared to the square lattice.

Experimental measurements of the shell-side mass transfer coefficient in fiber bundles are influenced by entry effects as well as irregularities within the bundle that induce cross flow. As a result, experiments often deviate from the assumption of fully developed, purely axial flow and typically reveal a certain degree of Reynolds number dependence in the Sherwood number [82].

4.1.6 Results for cross flow

In cross flow, a driving pressure gradient was applied only within the cross-sectional plane, involving both x and y components. Both the Darcy permeability K_T and the Sherwood number Sh are expected to vary with changes in the cross flow Reynolds number Re_T and the cross flow attack angle θ. The simulation results reported in [75] predicted a complex behavior.

In the hexagonal lattice, the angular dependence of any quantity follows a 60° periodicity. However, it is sufficient to study θ only between 0 and 30°, as the range from 30° to 60° can be obtained through reflection about the 30° direction.

The dependence of the permeability on the flow attack angle is shown in **Figure 7**(a), which reports the polar chart of the Darcy permeability K_T for different values of the cross flow Reynolds number Re_T (10, 30, 50, 100). Up to $Re_T \approx 10$ there is practically no influence of θ: the fiber lattice is hydraulically isotropic and the flow is self-similar. At higher Re_T, as inertial effects become significant, also anisotropy does: K_T departs from the uniform trend and starts to depend on θ. K_T develops an absolute maximum for $\theta = 0°$ (or 60°) and a minimum for $\theta = 30°$, which are the directions of symmetry of the hexagonal lattice. As Re_T increases further ($Re_T > 50$), the maximum at 0° - 60° persists but a secondary maximum develops for $\theta = 30°$, while two minima appear for $\theta° \approx 15°$ and 45°.

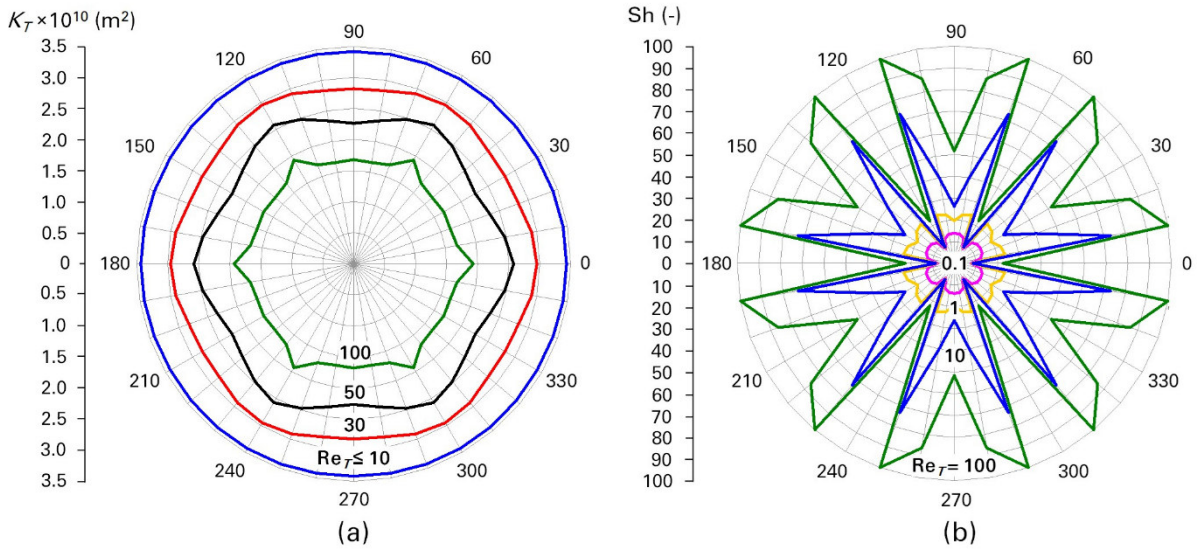

Fig. 7: Polar chart of the Darcy permeability K_T (a) and of the Sherwood number (b) for cross flow in a hexagonal lattice with ε=0.5 at different values of the Reynolds number Re_T. Data from [75].

The simultaneous dependence of mass transfer on Re_T and θ is evidenced in **Figure 7**(b), which reports the polar chart of the uniform wall mass flux Sherwood number, Sh, for four values of Re_T (0.1, 1, 10 and 100). Only at very low Reynolds numbers ($Re_T = 0.1$) Sh is about uniform with θ whereas, already at Re_T=1, it develops maxima at $\theta \approx 10$ and 50° ($+k\cdot 60°$) and two minima at $\theta = 0°$ and 30° ($+k\cdot 60°$) (symmetry directions).

The comparison of graphs (a) and (b) of **Figure 7** reveals that the hexagonal lattice remains hydraulically almost isotropic up to $Re_T \approx 10$ but, in regard to mass transfer, exhibits anisotropy at significantly lower Re_T values (0.1-1).

Figure 8 reports maps of the normalized velocity u^* and of the dimensionless concentration C^* (for urea) in the unit cell of a regular hexagonal lattice with $\varepsilon = 0.5$. The angle is $\theta = 30°$ and two different values of Re_T (0.001 and 0.01, respectively) are considered. These two quantities are defined here as

$$u^* = \frac{u}{\langle u_T \rangle} \tag{23}$$

$$C^* = \frac{\tilde{C} - C_b}{\bar{C}_w - C_b} \tag{24}$$

(refer to Section 4.1.1 for the various definitions).

Although maps (a) and (b) of u^* in **Figure 8** show that the flow is self-similar, the comparison of maps (c) and (d) for C^* shows how the fluid flow, even at low Re_T values, has a considerable impact on the scalar distribution. The thick line in the C^* maps represents the iso-concentration curve $C^* = 0$, i.e. $\tilde{C} = C_b$.

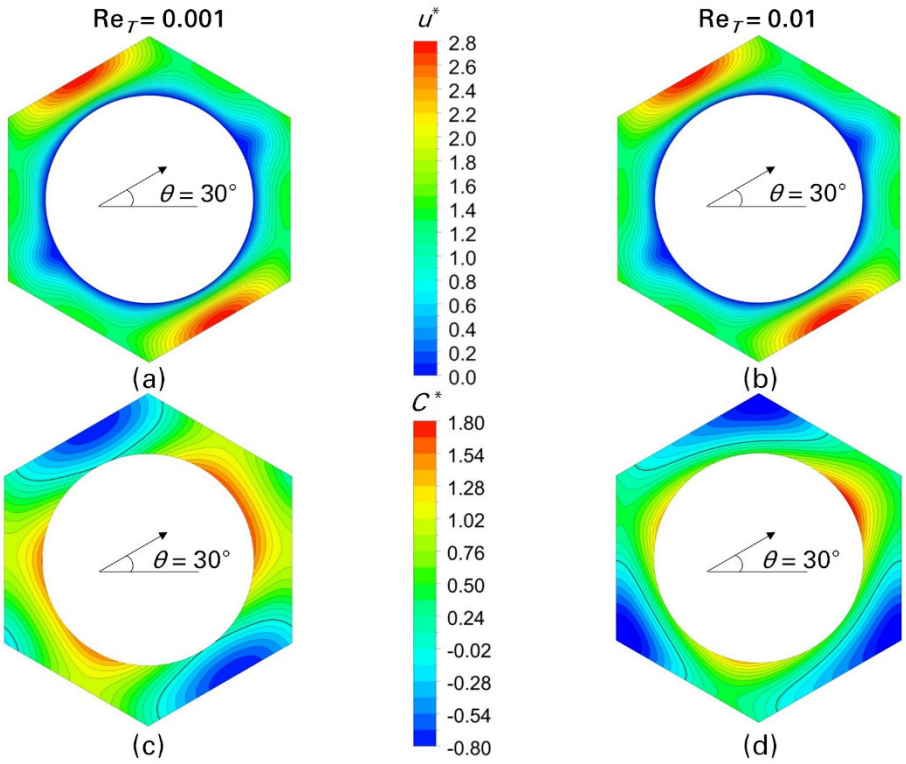

Fig. 8: Normalized velocity (a, b) and dimensionless concentration (c, d) in the unit cell of a hexagonal lattice with ε=0.5 for θ=30°: (a, c) Re_T=0.001; (b, d) Re_T=0.01. Reproduced (adapted) from [75], with permission from Elsevier (2021).

At Re_T = 0.01, map (d), the concentration at the wall consistently exceeds C_b. Otherwise, at very low Re_T = 0.001, map (c), the iso-line $\tilde{C}=C_b$ intersects the wall, resulting in some regions where $C_w>C_b$, others where $C_w<C_b$, and some points where $C_w=C_b$. In this case, the concentration distribution is nearly symmetrical between the upstream and downstream regions of the wall. However, at Re_T=0.01, advection disrupts this symmetry, resulting in a distinctly asymmetric scalar distribution. This is attributable to the high Schmidt number (423): the transverse Péclet number, $Re_T \cdot Sc$, is 0.423 in case (c) and 4.23 in case (d). Although these values are low, they are not insignificant. Even as the cross flow Reynolds number approaches zero, the concentration distribution does not align with the centro-symmetric configuration expected in pure diffusion or purely axial flow. On the contrary, the scalar distributions along

the flow direction and its perpendicular direction remain distinctly different. The intricate manner in which the cross flow distorts the iso-concentration curves accounts for the complex and non-monotonic relationship between the Sherwood number and Re_T, as illustrated in **Figure 7**(b).

The efficiency of solute transfer from the lumenside compartment to the dialysate, and thus the magnitude of the Sherwood number, is closely tied to the shape of the iso-concentration profiles for various cross flow attack angles. For example, **Figure 9** shows simplified concentration maps for three angles (0°, 15° and 30°) at Re_T=1. For clarity, a section of the lattice comprising seven periodic unit cells is illustrated. Regions where $C<C_b$ are shown in black, while regions in which $C>C_b$ are in red.

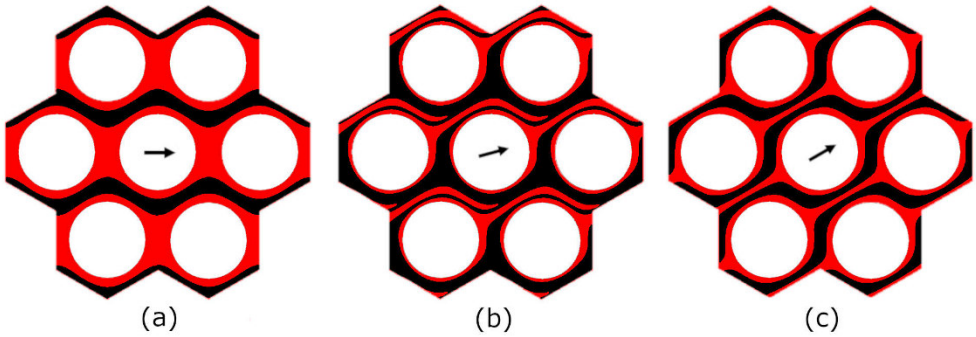

Fig. 9: Simplified concentration maps in a hexagonal lattice at Re_T=1, uniform wall mass flux and three different flow attack angles: (a) θ=0°; (b) θ=15°; (c) θ=30°. Red regions: $C>C_b$; black regions: $C<C_b$. The arrows denote the mean cross flow direction. Reproduced (adapted) from [75], with permission from Elsevier (2021).

At θ=0°, the wake with high concentration formed downstream of each fiber merges directly with the wake of the following fiber, resulting in a wide area of high concentration that impairs mass transfer. A comparable effect is observed, albeit to a lesser extent, at θ=30°. Conversely, at θ=15°, a direction that does not align with the lattice symmetry, the high concentration wake meanders around the fibers before eventually merging with the bulk flow. This significantly thins the concentration boundary layer and lowers the mean concentration at the fiber wall, leading to an improvement in mass transfer efficiency.

4.2 Non–ideal phenomena: effects of non–uniform and random fiber distributions

A common issue of haemodialyzers and, more in general, of hollow-fiber membrane contactors, is the management of shell-side non-ideal flow phenomena originating from the

non-uniform fibers distribution. The most common one, usually named in the literature as **channelling** [83, 84], occurs when the dialysate flows mainly through preferential passages of the bundle while in some regions the fluid is essentially stagnant. As reported, among others, by Bao and Lipscomb [85, 86], this phenomenon is observed in axial, cross- and mixed flow across non-uniform bundle distributions. Recently, several researchers have dealt with this topic. Sun et al. [87] investigated the influence on the performance of an axial-flow hollow fiber contactor presenting a radially non-uniform porosity between the core and peripheral regions of the bundle. Also Cancilla et al. numerically studied the effects of a non-uniform porosity on shell-side flow and mass transfer in both axial-flow [88] and cross-flow [89] conditions. The most noteworthy conclusion is that, in axial flow, non-uniformity produces a significant rise of the Darcy permeability and an even larger drop of the mass transfer coefficient. In cross-flow the behaviour is more complex, being observed a more important dependence both on the cross-flow attack angle and on the Reynolds number considered.

Figure 10 shows a cross-sectional view of a hollow fiber bundle for haemodialysis.

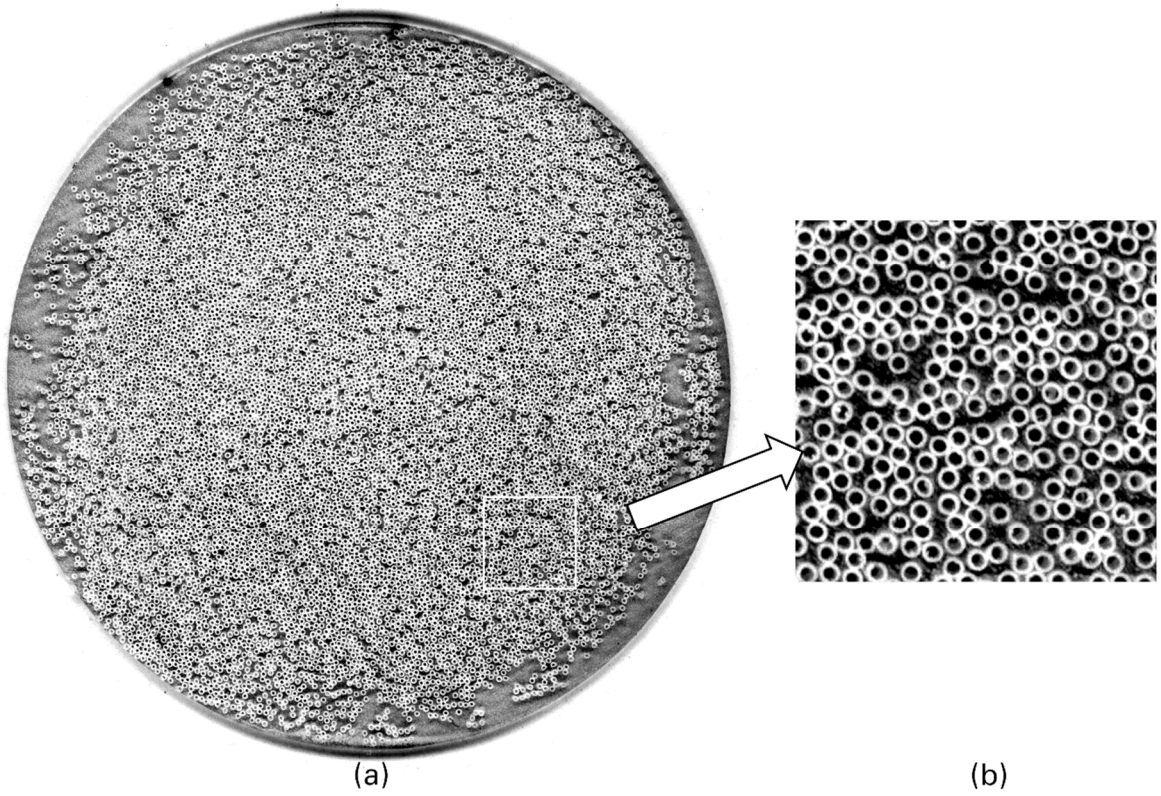

Fig. 10: Scanned images of a cross section of a real hollow fiber bundle used in a commercial haemodialyzer (Clearum™ HS Series high flux dialyzer, manufacturer: Medtronic®): (a) entire bundle (diameter ~40 mm, ~10,000 fibers, mean porosity ~0.5); (b) detail of a 5×5 mm square portion, exhibiting the non-uniform fiber distribution.

689 The peripheral regions, close to the cylindrical housing of the contactor, exhibit an
690 appreciably lower packing density compared to the central one. Even within the central regions,
691 although this displays a more uniform distribution, scattered gaps intermingled with clusters of
692 densely packed fibers can be observed, see magnification in **Figure 10**(b). Similar insights were
693 also reported by Frank et al. [90].
694 In axial flow, simulations for random clusters of fibers predicted values of f_z which follow
695 almost exactly a Re_z^{-1} trend, as already observed for the regular lattices in Section 4.1.5. The
696 Darcy permeability K_z increases by 1.85 times with respect to the hexagonal lattice and 1.47
697 times with respect to the square lattice at the same porosity. In regard to mass transfer, the value
698 of the Sherwood number is constant as Re_z increases, as expected in axial flow. Notably, as
699 pointed out by Bao and Libscomb [86], results for random fiber arrangements show that mass
700 transfer coefficients decrease dramatically in the fully developed region: values of Sh predicted
701 for random distributions are only 5-10% of those predicted for regular lattices. This large drop
702 is due to high flows through regions of the bundle characterized by high local porosity
703 (channelling). Similar conclusion was also obtained by the present authors [88], who studied
704 the channelling phenomenon using a simplified approach.
705 In cross flow conditions, random clusters of fibers behave as an orthotropic medium at low
706 Reynolds numbers and their permeability polar chart changes little in amplitude, shape and
707 orientation at higher Reynolds numbers. The amount of anisotropy of random distributions is
708 very large only for small clusters (~16 fibers) and decreases with the number of fibers, until it
709 becomes negligible for clusters embedding more than 100 fibers. This scale-dependence of the
710 anisotropy should be kept in mind when choosing a finite cluster of random fibers as
711 computationally representative of a much larger set. Of course, ensemble averaging over a
712 sufficient number of realizations destroys anisotropy. Ensemble averaged values of the Darcy
713 permeability exhibited a significant decrease with respect to the values computed for both
714 square and hexagonal regular lattices: notably, the lower the porosity, the highest the decrease.
715 On the other hand, at ε = 0.8-0.9, permeabilities computed for random clusters start to coincide
716 with those for regular arrays [91-95]. In regard to mass transfer, random realizations of 81 fibers
717 exhibited a quite isotropic polar chart of the average shell-side Sherwood number. At ε = 0.5 (a
718 typical value for most commercial haemodialyzers), Sh varies in a narrow range of values,
719 exhibiting a reduction of ~ 20-50% with respect to the angle-averaged value predicted for
720 regular lattices. As noted for hydrodynamics, ensemble averaging over an adequate number of
721 realizations destroys such anisotropy.

5. Module-scale 3–D porous media models

The most effective method for modelling haemodialyzers is likely the porous media approach. This method involves treating one or both fluids as moving through anisotropic porous media, as described by Darcy's law. Hydraulic permeabilities and mass transfer coefficients are obtained either through numerical simulations of a single fiber or based on experimental data. For example, Lemanski and Lipscomb [96] used literature values for the Darcy permeability [97, 98] in regular fibers arrays. They performed a theoretical 2-D analysis of shell-side flow and its influence on mass transfer neglecting ultrafiltration. Liao et al. [99] addressed this limitation, by incorporating both convection and diffusion into their 2-D model. The shell-side was treated as a porous medium with Darcy permeabilities derived from experiments as well as membrane properties. Eloot et al. [100] implemented a CFD model of a haemodialyzer, defining the blood and dialysate compartments as two porous media with uniform axial and radial permeabilities. Other 2-D models using the concept of interpenetrating porous media include those developed by Łabęcki et al. [101], Lemanski and Lipscomb [102] and Ding et al. [103]. Ding et al. [104] developed a 3-D model of a haemodialyzer to more accurately capture the effects of inlet and outlet headers and the interaction between blood and dialysate flows. Darcy permeabilities were sourced from existing literature; the authors used a global mass transfer coefficient obtained from experimental data in the literature.

In this section, starting from the concept of two interpenetrating porous media, the model of fluid flow and mass transfer in hollow fiber modules for haemodialysis proposed by Cancilla et al. [105] is reported. The model is based on two-scale approach. Predictions from single-fiber models at a small-scale level (refer to Section 4) were translated into equivalent properties for a porous medium. Simulations at the module-scale were then carried out to predict the three-dimensional flow fields and solute concentrations in both the blood and dialysate compartments of a haemodialyzer.

5.1 Small-scale CFD correlations

The main results that can be carried over from the unit cell-scale model discussed in Section 4 to the porous media model of the whole haemodialyzer are the shell-side axial and cross flow Darcy permeabilities and the shell-side Sherwood number.

In regard to Darcy permeabilities K_z and K_T, suitable two-parameters correlations derived by fitting in the range $0.2<\varepsilon<0.8$ the CFD results reported in [106] are:

$$K_z = (10^{-4}\, d^2)\cdot\exp(9.2\varepsilon) \tag{25}$$

$$K_T = (1.66\cdot 10^{-1}\, d^2)\cdot\varepsilon^5 \tag{26}$$

For the shell-side Sherwood number, a correlation of the CFD results reported in Section 4 for regular hexagonal lattices with ε=0.5 is:

$$\mathrm{Sh} = a\,(1 + b\cdot \mathrm{Re}_T^{\,c}) \tag{27}$$

For a=9.85, b=1.41 and c=0.38, Eq. (27) align well with the CFD results of the single-fiber model within the Reynolds number range Re_T=0.005-50. The coefficient a is chosen to ensure that, at Re_T=0, the correlation yields the value of Sh for purely axial flow. The Sherwood numberestimated by Eq. (27) represents an average value across all possible cross-flow directions relative to a hexagonal lattice. The results reported in Section 4 showed that at the low Reynolds numbers (approximately 0.1-1) typical of a real haemodialyzer, the orientation of the cross flow has limited effects on the Sherwood number.

For the lumen side Sherwood number, a value of 4 was adopted as a compromise between the exact values for uniform wall concentration and uniform wall mass flux in circular pipes, which are 3.66 and 4.36, respectively [107].

5.2 Porous media approach

The fluid on each side (whether blood or dialysate) was modelled as flowing through its own distinct equivalent porous medium. Each porous medium was characterized by its bundle porosity ε and the addition of the following momentum source terms to the right-hand side of the momentum (Navier-Stokes) equations:

$$S_{M,T} = -\frac{\mu}{K_T}\langle u_T \rangle \tag{28}$$

$$S_{M,z} = -\frac{\mu}{K_z}\langle u_z \rangle \tag{29}$$

in which $\langle u_T \rangle$ and $\langle u_z \rangle$ are the superficial velocities along the T and z directions, respectively. For the Darcy permeabilities K_z and K_T, equations (25) and (26) were adopted.

To account for ultrafiltration effects, the mass source term S_M (kg m^{-3} s^{-1}) was added to the right-hand side of the continuity equation:

$$S_M = \pm \frac{A_{ext}}{V_{tot}} \rho L_p \left(p_B - p_D - p_{onc} \right) \tag{30}$$

where the "plus" sign is used for dialysate and the "minus" sign for blood; A_{ext} is the total external surface area of the hollow fibers, V_{tot} is the total volume of the module, L_p is the hydraulic permeability of the membrane, p_B and p_D are the pressures in the blood and dialysate compartments, respectively, and p_{onc} is the oncotic pressure of the blood proteins. Likewise, to account for solute mass flux, the source term S_C (in mol m^{-3} s^{-1}) was added to the right-hand side of the scalar transport equation for the solute:

$$S_C = \pm \frac{A_{ext}}{V_{tot}} j \tag{31}$$

with, again, the "plus" sign applying to dialysate and the "minus" sign to blood. The total molar flux of solute per unit membrane area, j, expressed (in mol m^{-2} s^{-1}), is:

$$j = L_p \cdot \left(p_B - p_D - p_{onc} \right) \cdot \left(1 - \sigma \right) \cdot C_M + U \cdot \left(C_B - C_D \right) \tag{32}$$

The first term of Eq. (32) accounts for the convective contribution to mass transport due to ultrafiltration. Here, σ is Staverman's reflection coefficient and C_M represents the concentration of the solute in the fluid passing through the membrane. Notably, C_M can be expressed as the arithmetic mean $(C_B+C_D)/2$ [99] or the logarithmic mean $(C_B-C_D)/\ln(C_B/C_D)$ [104] of the lumen- and shell-side bulk concentrations C_B, C_D. An additional approach could be to equate C_M with the upstream bulk concentration, specifically C_B if the ultrafiltration flux is from blood to dialysate, or C_D if it is the reverse. Comparing these alternatives revealed no substantial differences in the results.

The second term of Eq. (32) accounts for diffusive mass transfer, driven by the concentration gradient. U denotes the overall mass transfer coefficient, defined as:

$$U = \frac{1}{\frac{1}{k_B} + \frac{1}{k_M} + \frac{1}{k_D}} \tag{33}$$

in which k_B, k_M and k_D represent the mass transport coefficients for blood, membrane and dialysate, respectively. Rigorously, Eq. (33) is applicable to a planar membrane configuration. However, it is widely used in the literature for cylindrical fiber geometries as well, with the coefficients k_B and k_M incorporating the necessary geometric adjustments.

The mass transfer coefficient on the blood-side, k_B, can be computed using the following

formula:

$$k_B = \mathrm{Sh}_B \frac{D_B}{d_i} \tag{34}$$

where D_B is the diffusivity of the solute in the blood, d_i is the internal fiber diameter and Sh_B is the Sherwood number on the blood-side.

The mass transfer coefficient on the dialysate-side, k_D, was calculated as:

$$k_D = \mathrm{Sh}_D \frac{D_D}{d_h} \tag{35}$$

in which d_h is the fiber bundle hydraulic diameter, D_D is the diffusivity of the solute in the dialysate and Sh_D is Sherwood number on the dialysate-side. For Sh_D, Eq. (27) was used, expressing it as a function of the shell-side cross-flow Reynolds number Re_T and averaging over all possible cross flow directions.

The term k_M in Eq. (33) denotes the membrane's diffusive permeability for the specified solute. This parameter depends on the membrane structure, composition and thickness.

5.3 Estimation of mass transport resistances

In Eq. (33) the three components (blood, dialysate and membrane) are treated as in a resistance in series model. Identifying the "controlling" step, i.e., the one that most significantly contributes to the overall resistance to mass transfer, is crucial for understanding and optimizing solute removal. To perform a preliminary estimation of the mass transport resistances, values of k_M for commercial polyphenylene membranes relative to two solutes (urea and B12 vitamin) are considered. Such data are reported, together with the hydraulic permeability L_p, in **Table 4**; for the physical fluids and solutes properties, data are reported in **Table 5**.

Tab. 4: Membrane properties used in the simulations by Cancilla et al. [105].

Membrane property	Urea	B12 vitamin
k_M (m s^{-1})	$(1.1 \pm 0.2) \times 10^{-5}$	$(3.1 \pm 0.2) \times 10^{-6}$
L_p (m s^{-1} Pa^{-1})	$(6.6 \pm 0.4) \times 10^{-11}$	

Tab. 5: Fluids and solutes properties used in the simulations by Cancilla et al. [105].

Fluid	Density, ρ (approx, kg m^{-3})	Viscosity, μ (Pa s)	Diffusivity, D (m^2 s^{-1})	Schmidt number, Sc (-)	Inlet concentration, C_i (mol m^{-3})	Inlet volume flow rate, Q (mL min^{-1})
Blood	1000	3.5×10^{-3}	7.4×10^{-10} (urea) 4.0×10^{-10} (B12)	4730 8750	20 (urea) 3×10^{-2} (B12)	300
Dialysate	1000	7.62×10^{-4}	1.8×10^{-9} (urea) 5.0×10^{-10} (B12)	423 1524	0	500

Estimates are conducted for membranes having internal and external fiber diameters d_i = 200 μm and d = 260 μm, respectively, and a bundle porosity ε = 0.5. Sherwood numbers of 4 for the blood-side and 9.85 for the dialysate-side, corresponding to axial flow, are considered. Results of such estimates are given in **Figure 11**. According to the literature [44, 54], the membrane accounts for more than half of the resistance to mass transport in current high-flux modules. This is particularly evident for high–molecular–weight solutes like B12 vitamin (MW = 1355 Da [108]), where membrane resistance is the predominant one. For smaller solutes such as urea (MW = 60 Da [108]), the resistance within the blood compartment becomes more significant.

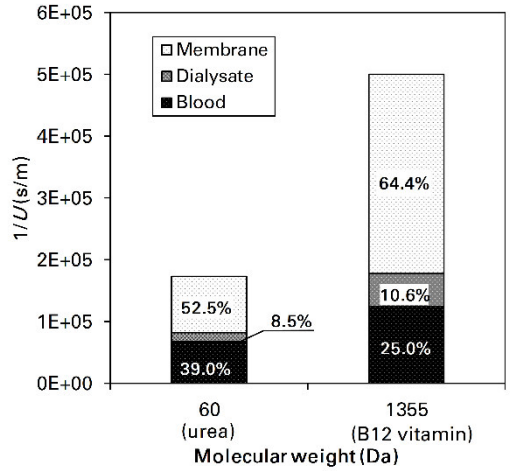

Fig. 11: Component of the total mass transfer resistance (in s/m) for urea and B12 vitamin. Reproduced (adapted) from [105], with permission from Elsevier (2022).

5.4 Computational domain and simulation strategy

Figure 12 reports the cylindrical geometry simulated by Cancilla et al. [105]. The computational domain, representative of a commercial haemodialysis module, includes eight

inlets and eight outlets for dialysate flow, simulating the presence of a fluid distributor. Arrows indicate the flow direction, with red representing blood and blue denoting dialysate.

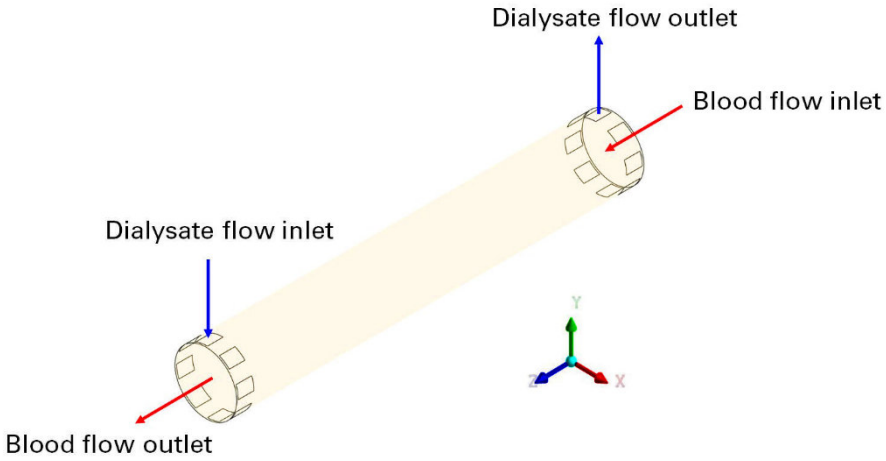

Fig. 12: Geometry of the 3-D computational domain for the simulated module. Reproduced (adapted) from [105], with permission from Elsevier (2022).

The model was implemented using the finite volume code Ansys-CFX 18® [109]. Blood and dialysate were simulated as separate fluids flowing through two different porous media that occupy the entire internal volume of the module. The two fluids interact by transferring both the solution and solutes between them. This required an iterative approach: flow rates and solute concentrations on both the blood and the dialysate sides were interconnected through proper sink/source terms that represent solute exchange. These values were recalculated alternately until the results converged.

Figure 13 illustrates the flow chart of the computational procedure. Here and below, the subscripts "*B*" and "*D*" are for blood and dialysate, respectively.

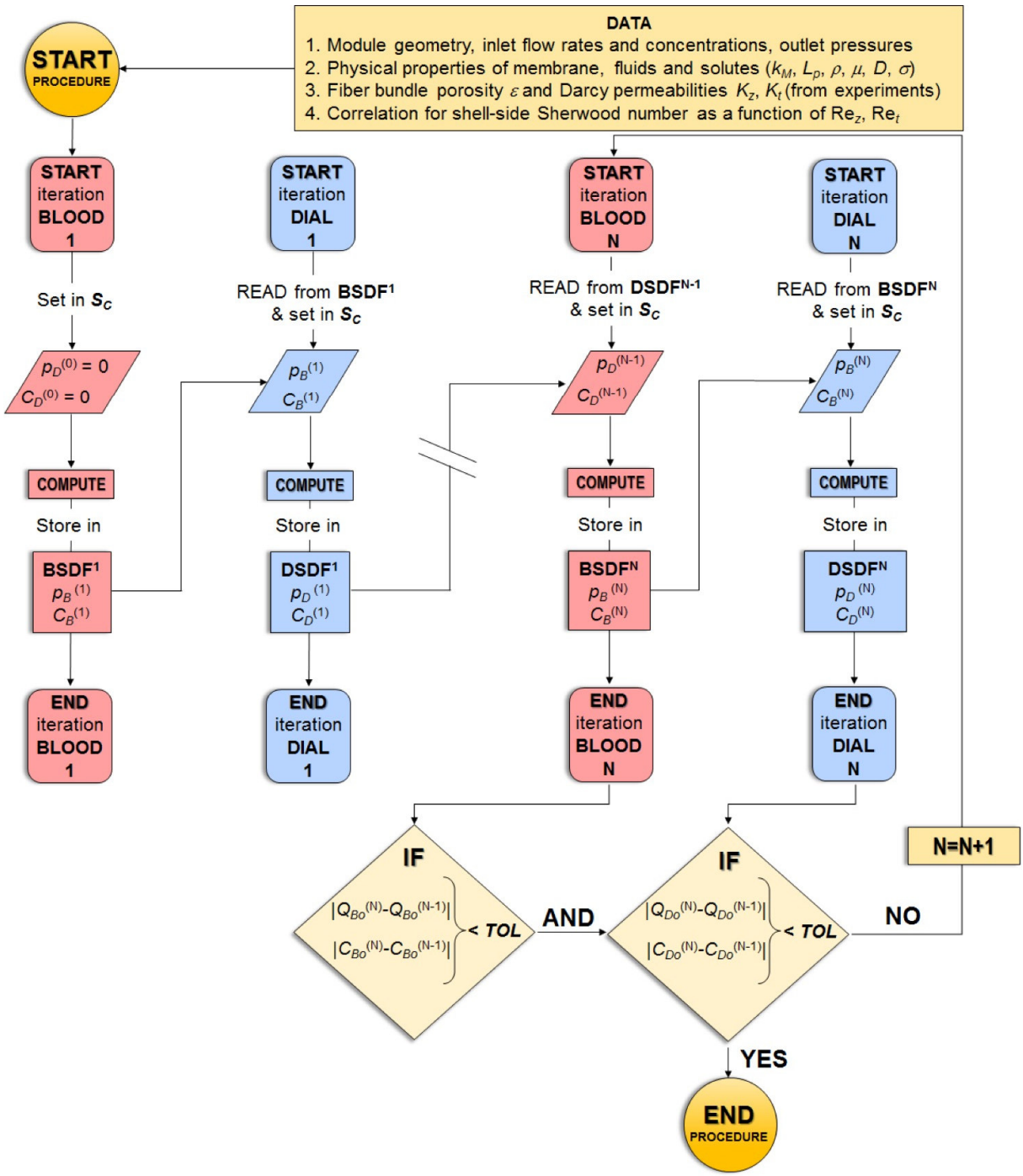

Fig. 13: Flow chart illustrating the computational procedure for the porous media model. Reproduced from [105], with permission from Elsevier (2022).

The two fluid were described by the relevant physical properties (ρ, μ, D), the inlet volume flow rate (Q) and the inlet concentration (C_i), as shown in **Table 5**, along with their specific inlet and outlet configurations. It was assumed that each fluid flowed through a porous medium characterized by porosity (ε), longitudinal permeability (K_z) and cross flow permeability (K_T), as defined by Eqs. (25) and (26). The Sherwood number on dialysate-side was calculated using

Eq. (27).

The solute markers were urea and B12 vitamin, with Staverman's reflection coefficients σ set at 0 and 0.15, respectively. The membrane's hydraulic permeability L_p and the diffusive permeabilities k_M for these solutes were as in **Table 4**.

In regard to boundary conditions, a no–slip wall condition with zero mass flux was applied to the internal cylindrical shell surface. Outlet conditions for both blood and dialysate were set by pressure, while inlets were defined by flow rates. Outlet pressure of the dialysate was set to zero (relative) while, for the blood, it was adjusted to achieve a 10 mL/min ultrafiltration flow rate. Both fluids used the same computational grid.

The procedure begins with the first iteration for the blood-side (BLOOD 1). In this step, in the mass transfer source term S_C for blood (using a negative sign in Eq. (31)) assumes zero dialysate-side pressure p_D and concentration C_D. After completing this iteration, the predicted blood-side pressure p_B and concentration C_B distributions are saved in the Blood-Side Data File "BSDF[1]".

The next step of the simulation procedure (DIAL 1) focuses on the dialysate side. In this iteration, the mass transfer source term S_C for the dialysate (using a positive sign in Eq. (31)) uses the blood-side pressure p_B and concentration C_B retrieved from the previously saved Blood-Side Data File. Once this iteration is complete, the resulting dialysate-side pressure p_D and concentration C_D distributions are saved in the Dialysate-Side Data File "DSDF[1]".

In the following iterations (BLOOD N – DIAL N), each side retrieves the most recent concentration and pressure fields for the opposite side from the corresponding saved file. After updating its own pressure and concentration fields, each side records these results in its respective data file.

Convergence is reached when the differences in outlet flow rate and solute concentration between successive iterations for both blood and dialysate drop below a specified tolerance (*TOL*). Typically, convergence to within 0.5% was attained within 6 to 9 couples of iterations.

5.5 Model validation

To validate the model, the predicted clearance values for urea and B12 vitamin were compared with experimental clearances measured in commercial modules. Experiments referred to PHYLTHER® HF SD15 (membrane area 1.5 m^2) and SD17 (membrane area 1.7 m^2) modules commercialized by Medtronic® using a saline solution instead of blood. Hence, simulations were performed by substituting the blood in the lumen with a fluid matching the

physical properties of the saline solution used in the experiments and setting the corresponding oncotic pressure to zero. The dialysate flow rate was set at 500 mL/min and simulations were conducted with lumen-side flow rates of 200, 300 and 400 mL/min. As in the experiments, the ultrafiltration flow rate was held constant at 10 mL/min. The data for membrane diffusive permeability and hydraulic permeability were those reported in **Table 4**.

Figure 14 presents a comparison between the solute clearances predicted by the model and the corresponding experimental data.

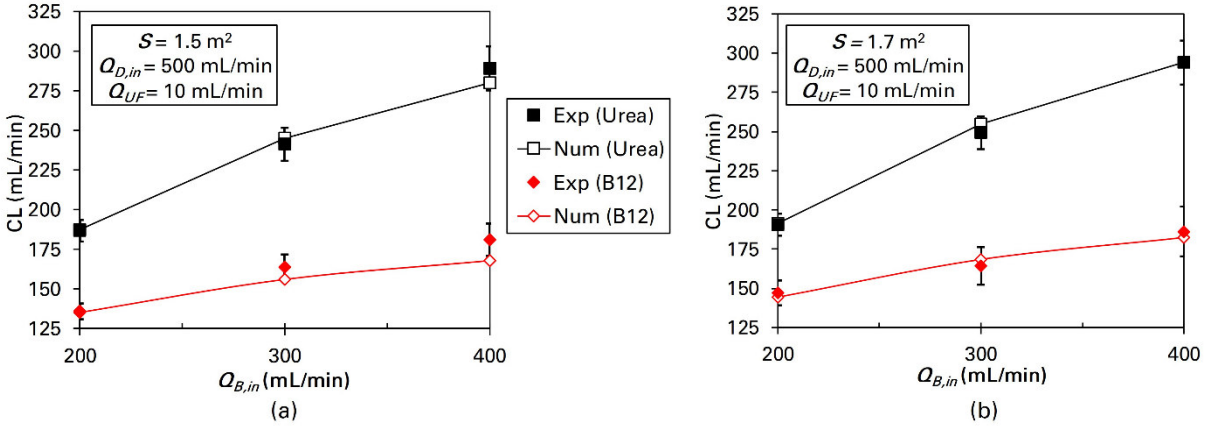

Fig. 1: Clearance of urea (black) and B12 vitamin (red) as functions of the inlet blood flow rate for the 1.5 m^2 (a) and the 1.7 m^2 (b) modules. Model predictions (solid lines and hollow symbols) are compared with experimental results (solid symbols) provided with dispersion bars. Reproduced (adapted) from [105], with permission from Elsevier (2022).

Clearance rises with the blood flow rate and with the module size. Model predictions consistently fall within the range of the experimental data. For all modules and solutes, the closest match to experimental results is observed at the lowest blood flow rate of 200 mL/min. The greatest deviation occurs for B12 vitamin with the 1.5 m^2 module at a blood flow rate of 400 mL/min.

5.6 Fluid flow and solute concentration distributions

The present section reports results obtained with the porous media model for a baseline scenario: blood and dialysate flow rates were set at 300 and 500 mL/min, respectively, with an ultrafiltration flow rate fixed at 10 mL/min. Membrane and fluids properties were as in **Table 4** and **Table 5**, respectively. The oncotic pressure in the blood was set at 3700 Pa (~28 mmHg as in typical human blood [110]). For the baseline scenario, the model predicts clearances of ~257 mL/min for urea and ~172 mL/min for B12 vitamin. **Figure 15** illustrates the pressure

distributions within both compartments of the module. Here, blood flows from right to left, while dialysate flows from left to right.

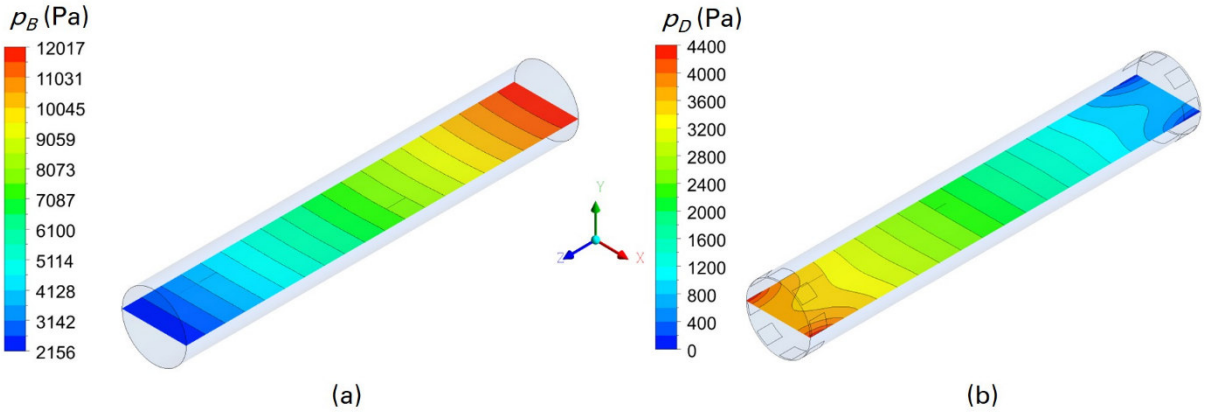

Fig. 25: Color maps of pressure distribution in the *zx* mid-plane. (a) blood side; (b) dialysate side. Reproduced (adapted) from [105], with permission from Elsevier (2022).

The pressure maps for both the blood and the dialysate sides display a linear gradient along most of the module length, consistent with observation by Osuga et al. [111]. The pressure drops between the inlets and outlets were ~9860 Pa for blood and ~4400 Pa for dialysate. This disparity arises from the differences in the fluid properties, blood being about 5 times more viscous than dialysate, and the variations in their respective axial Darcy permeabilities. The blood outlet pressure was set to 2156 Pa to obtain an ultrafiltration flow rate of 10 mL/min.

Figure 16 reports the corresponding concentration distributions of urea and B12 vitamin. The maps show a mainly axial concentration stratification in both the blood and the dialysate, with a superimposed radial gradient. This gradient is most pronounced near the dialysate inlet and blood outlet regions, due to the peripheral locations of the dialysate inlet-outlet ports. These findings align qualitatively with the results reported by Ding et al. [104].

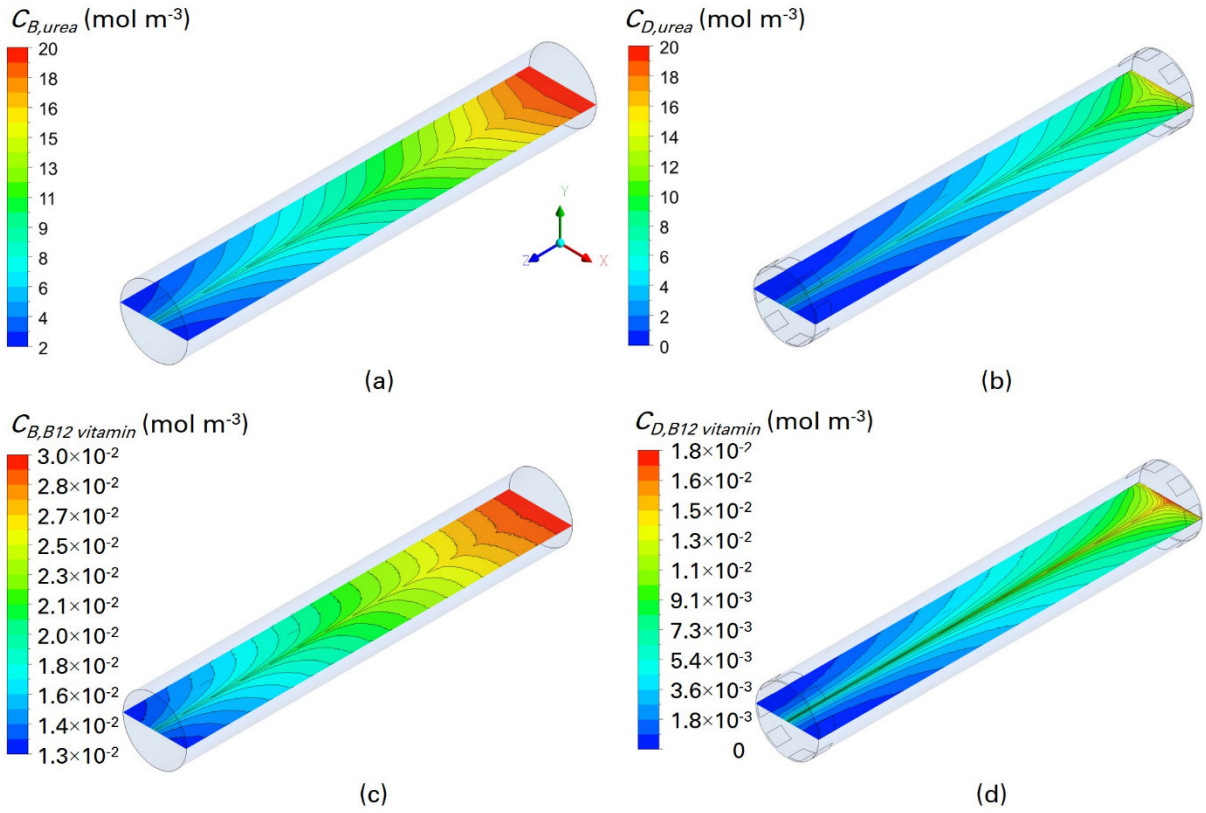

Fig. 3: Color maps of solute concentration in the *zx* mid-plane. Left column: blood side; right column: dialysate side. Solute: (a, b) urea; (c, d) B12 vitamin. Reproduced (adapted) from [105], with permission from Elsevier (2022).

5.7 Parametric sensitivity assessment

A parametric analysis was performed to assess the sensitivity of the results to different parameters: the membrane's diffusive permeability, the oncotic pressure, the ultrafiltration and the dialysate flow rates.

At first, a baseline scenario was simulated. Subsequently, the effect of varying each parameter individually, while keeping all other parameters constant, was assessed to determine its impact on the results.

The bar graphs in **Figure 17** condense, in terms of solute clearance, the results of the parametrical study. For the two solutes, urea (a) and B12 vitamin (b), the baseline scenario result is represented by the white bar, while the other bars correspond to each variant analyzed.

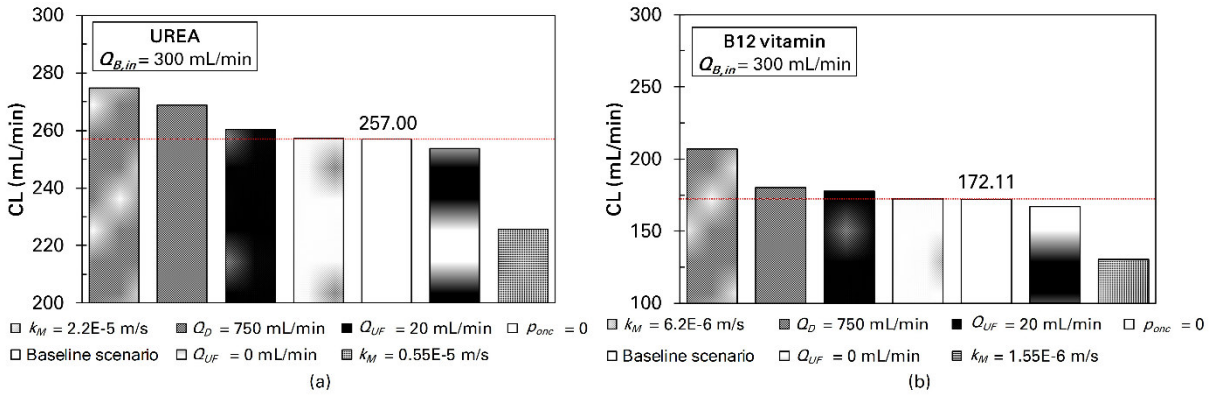

Fig. 17: Values of the solute clearances obtained in the parametrical analysis. Solute: (a) urea; (b) B12 vitamin. Reproduced (adapted) from [105], with permission from Elsevier (2022).

The membrane's diffusive permeability, k_M, is the most effective parameter. Doubling k_M results in a clearance increase of ~7% for urea and ~20% for B12 vitamin. On the other hand, halving k_M leads to a reduction in solute clearances of ~12% (urea) and ~24% (B12 vitamin). The dialysate flow rate, Q_D, is the second most effective parameter. An increase in Q_D from 500 to 750 mL/min results in a roughly 4% rise in clearance for both solutes. The ultrafiltration flow rate, Q_{UF}, has a relatively minor effect on clearance, even though it significantly affects hydrodynamics, particularly in term of backfiltration. A ±10 mL/min change in Q_{UF} from the baseline value of 10 mL/min results in a clearance variation of ~±1% for urea and ~±3% for B12 vitamin. Including or excluding plasma proteins (oncotic pressure) in the blood had a negligible influence on solute clearance for both solutes.

Lastly, the possibility of enhancing a module performance by employing geometries alternative to the typical cylindrical one has been investigated by the present authors in a dedicated work [112] confirming the effectiveness of the commercial module design for the currently available membrane properties.

6. Conclusions and Outlook

This chapter has provided an overview of the mathematical modelling approaches employed to study commercial haemodialyzers, which consist of cylindrical modules filled with hollow fiber.

A brief overview of healthy kidney function and its pathologies is provided to help the reader identify the essential functions that replacement treatment must replicate and the key reasons for its necessity. Subsequently, the chapter presents hollow fiber membrane processes for renal treatments of uremic patients, along with a classification of hemodialysis membranes

based on the polymer material composition.

The discussion emphasized the importance of accurately representing fluid dynamics, solute transport and membrane characteristics to effectively predict haemodialyzer performance. Small-scale CFD models, which predict fluid flow and mass transfer in small domains, including either a single fiber (using a unit cell approach to simulate regular lattices of straight fibers) or a limited number of fibers, have been reported. These models represent the first level of a more complex multiscale modelling tool developed to understand fundamental fluid dynamics parameters and solute transport phenomena within a haemodialysis module. Additionally, simulations of small portions of the bundle can help investigate fluid flow and mass transfer in non-uniform fiber arrays. Simulations of random fiber arrangements are also briefly discussed, with evaluations of the relevant effects of randomness on hydrodynamics and mass transfer.

The porous media approach has been explored, highlighting its applications and current limitations. Sensitivity analysis demonstrates that parameters such as the membrane's diffusive permeability and the dialysate flow rate significantly influence solute clearance, whereas the impact of ultrafiltration flow rate and oncotic pressure is comparatively minor. Current dialyzers are likely operating near their performance limits in terms of configurations and operating conditions, suggesting that optimizing these variables may be offer limited benefits. Future improvements in clearance performance will probably depend on the development of new membranes technologies with much higher diffusive permeability. The interpenetrating-fluid, porous-media model offers versatility and could be adapted for other processes involving heat or mass transfer between separated fluids.

Moving forward, future research could focus on refining model accuracy by incorporating more complex factors. The modelling tools presented in this chapter could serve as a foundation step for more advanced models. For example, developing flow conditions deserves more accurate investigations, and also simulations under the fully developed assumption are currently only partially complete, hindering a complete understanding. A thorough investigation of the effects of the bundle non-uniformity and a detailed parametric study of random fiber arrangements would be beneficial. Enhancing the porous media model with permeability and mass transfer correlations tailored for random distributions of hollow fibers could more accurately capture the complexities of real fiber bundles. Additionally, efforts are being made to account for the non-uniform porosity distribution in actual bundles, with a focus on radial variations. Simulating geometries with different local porosity values, directly derived from

experimental cross-section images of real bundle, could better reproduce the behavior of actual bundles. This is increasingly feasible thanks to advancement in image acquisition techniques.

Another significant area of focus is the inclusion of fiber undulation effects, which impact hydraulic permeability and mass transfer coefficients, allowing for a more realistic simulation of the fluid dynamics within the dialysis module. Currently, many companies manufacturing haemodialysis modules are trending towards the use of self-structured (undulated) fiber bundles. These fiber bundles exhibit interesting behaviors, ensuring adequate clinical performance. An in–depth experimental investigation, beyond the current literature, is advisable to fully characterize modules using self-structured hollow fiber bundles. This exploration could provide valuable insights into their performance and help refine existing models for better predictive accuracy.

Therefore, through the synergistic integration of increasingly detailed modelling tools and advancements in membrane science technology, the objective of developing more accurate models could soon be realized.

References

[1] Farquhar MG, Kanwar YS. Functional Organization of the Glomerulus: State of the Science in 1979. In: Michael AF and Cummings N, Eds. Immune Mechanisms in Renal Disease. Plenum Press, New York 1982; pp.1–35.

[2] Huang W, Chen YY, He FF, Zhang C. Revolutionizing nephrology research: expanding horizons with kidney-on-a-chip and beyond. Front. Bioeng. Biotechnol. 2024; 12:1373386.

[3] Navar LG, Bell PD, White RW, Watts, RL, Williams, RL (1977) Evaluation of the Single Nephron Glomerular Filtration Coefficient in the Dog. Kidney Int 1977; 12:137–49.

[4] Van Damme M, Bergmann P, Lambert PP. A Three Layer Model to Estimate Charge Densities in the Glomerular Wall. In: Lambert PP, Bergmann P and Beauwens R, Eds. The Pathogenicity of Cationic Proteins. Raven Press, New York 1983; pp.223–36.

[5] Farquhar MG. The Glomerulal Basement Membrane: A Selective Macromolecular Filter. In: Hay ED, Ed. Cell Biology of Extracellular Matrix. Plenum Press, New York 1981; pp.335–78.

[6] Farquhar MG, Courtoy PJ, Lemkin MC, Kanwar YS. Current Knowledge of the Functional Architecture of the Glomerular Basement Membrane. In: Kuhn K, Schone H and Timpl R, Eds. New Trends in Basement Membrane Research. Raven Press, New York 1982.

[7] Caulfield JP, Farquhar MG. Distribution of Anionic Sites in the Glomerular Basement Membranes. Their Possible Role in Filtration and Attachment. Proc Nat Acad Sci USA 1976; 73(6): 1646–50.

[8] Kanwar YS, Farquhar MG. Anionic Sites in the Glomerular Basement Membrane. 'In Vivo' and 'In Vitro' localization to the Laminae Rarae by Cationic Probes. J Cell Biol 1979; 81:137–53.

[9] Venkatachalam MA, Rennke HG. Glomerular Filtration of Macromolecules: Structural, Molecular and Functional Determinants. In: Leaf A, Giebisch G, Bolis L and Cornini S, Eds. Renal Pathophysiology. Raven Press, New York 1980; pp. 43–56.

[10] Deen WM, Bridges CR, Brenner BM. Biophysical Basis of Glomerular Permselectivity. J Memb Biol 1983; 71:1–10.

[11] Bayliss LE, Tookey-Kerridge M, Russell DS. The Excretion of Protein by the Mammalian Kidney. J Physiol 1933; 77:386–98.

[12] Chang RLS, Ueki IF, Troy JL, Deen WM, Robertson CR, Brenner BM. Permselectivity of the Glomerular Capillary wall to Macromolecules: II. Experimental Observations in the Rat. Biophys J 1975; 15:887–906.

[13] Rennke HG, Cotran RS, Venkatachalam MA. Role of Molecular Charge in Glomerular Permeability. Tracer Studies with Cationized Ferritin. J Cell Biol 1975; 67:638–46.

[14] Rennke HG, Venkatachalam MA. Glomerular Permeability: 'In Vivo' Tracer Studies with Polyanionic and Polycationic Ferritins. Kidney Int 1977; 11:44–53.

[15] Rennke HG, Venkatachalam MA. Glomerular Filtration of Proteins: Clearance of Anionic, Neutral and Cationic Horseradish Peroxidase in the Rat. Kidney Int 1978; 13:278–88.

[16] Brenner BM, Lawrence WE. Modern Concepts of Glomerular Permselectivity. In: Lambert PP, Bergmann P and Beauwens R, Eds. The Pathogenicity of Cationic Proteins. Raven Press, New York 1983; pp.183–205.

[17] Bohrer MP, Baylis C, Humes HD, Glassock RJ, Robertson CR, Brenner BM. Permselectivity of the Glomerular Capillary Wall. Facilitated Filtration of Circulating Polycations. J Clin Invest 1978; 61:72–8.

[18] Kanwar YS, Rosenzweig LJ. Altered Glomerular Permeability as a Result of Focal Detachment of Visceral Epithelium. Kidney Int 1982; 21:565–74.

[19] Gregor HP, Gregor CD. Synthetic Membrane Technology. Sci Amer 1978; 239:112–28.

[20] Jager KJ, Kovesdy C, Langham R, Rosenberg M, Jha V, Zoccali C. A single number for advocacy and communication-worldwide more than 850 million individuals have kidney diseases. Nephrol Dial Transplant 2019; 34(11):1803–05.

[21] United States Renal Data System. 2018 USRDS annual data report: Epidemiology of kidney disease in the United States. National Institutes of Health, National Institute of Diabetes and Digestive and Kidney Diseases, Bethesda, MD, 2018.

[22] Dialysis Market Size, Share & COVID-19 Impact Analysis, By Type (Products and Services), By Dialysis Type (Hemodialysis and Peritoneal Dialysis), By End User (Dialysis Centers & Hospitals and Home Care), and Regional Forecast, 2020-2027; Jun, 2020.

[23] Leaf A, Giebisch G, Bolis L, Gorini S, Eds. Renal Pathophysiology. Raven Press, New York 1980.

[24] Arnaout MA, Rennke HG, Cotran RS. Membranous Nephropathy. In: Stein JH, Ed. Contemporary Issues in Nephrology, Vol 9, Nephrotic Syndrome. Churchill Livingstone, New York 1982; pp.199–235.

[25] Olson JL, Rennke HG, Venkatachalam MA. Alterations in Charge and Size Selectivity barrier of the Glomerular Filter in Aminonucleoside Nephrosis in Rats. Lab Invest 1981; 44:271–9.

[26] Rennke HG. Charge and Size Selective Properties of the Glomerular Capillary Wall in Normal Rats and in Experimentally Induced Proteinuria. In: Lambert PP, Bergmann P and Beauwens R, Eds. The Pathogenicity of Cationic Proteins. Raven Press, New York 1983; pp.272–80.

[27] Vernier RL, Papermaster BW, Good RA. Aminonucleoside Nephrosis. I. Electron Microscopic Study of the Renal Lesions in Rats. J Exp Med 1959; 109:115–26.

[28] Robson AM, Gianagiacomo J, Keinstra RA, Naqvi ST, Ingelfinger JR. Normal Glomerular Permeability and its Modification by Minimal Change Nephrotic Syndrome. J Clin Invest 1974; 54:1190–9.

[29] Bohrer MP, Baylis C, Robertson CR, Brenner BM. Mechanism of Puromycin–Induced Defects in the Transglomerular Passage of Water and Macromolecules. J Clin Invest 1977; 60:152–61.

[30] Weening JJ, Rennke HG. Glomerular Permeability and Polyanion in Adriamycin Nephrosis in the Rat. Kidney Int 1983; 24:152–9.

[31] Barnes JL, Venkatachalam MA. Glomerular Interactions of Exogenous and Endogenous Polycations. In: Lambert PP, Bergmann P and Beauwens R, Eds. The Pathogenicity of Cationic Proteins. Raven Press, New York 1983; pp.281–93.

[32] Seiler MW, Rennke HG, Venkatachalam MA, Cotran RS. Pathogenesis of Polycation-Induced Alterations ("Fusion") of Glomerular Eipithelium. Lab Invest 1977; 36:48–61.

[33] Chang RLS, Robertson CR, Deen WM, Brenner BM (1975.a) Permselectivity of the Glomerular Capillary wall to Macromolecules: I. Theoretical Considerations. Biophys. Journal, Vol. 15, pp.861-886.

[34] Eisenbach GM, vanLiew JB, Boylan JW (1975) Effect of Angiotensin on the Filtration of Protein in the Rat Kidney: a Micropuncture study. Kidney Int., Vol. 8, pp.80-87.

[35] Baylis C, Deen WM, Myers BD, Brenner BM (1976) Effects of Some Vasodilator Drugs on Transcapillary Fluid Exchange in Renal Cortex. Amer. J. Physiol., Vol. 230, pp.1148-1158.

[36] Colton CK, Lysaght MJ. Membranes for hemodialysis. Replace Ren Funct by Dial 1996; 103–13.

[37] Lysaght MJ. Hemodialysis Membranes in Transition. Contrib.Nephrol. 1988; 61:1–17.

[38] Lysaght MJ. Evolution of hemodialysis membranes. Contrib Nephrol 1995; 113:1–10.

[39] Clark WR, Hamburger RJ, Lysaght MJ. Effect of membrane composition and structure on solute removal and biocompatibility in hemodialysis. Kidney Int 1999; 56(6):2005–15.

[40] Klinkmann H, Vienken J. Membranes for dialysis. Nephrol Dial Transplant 1995; 10(SUPPL. 3):39–45.

[41] Craddock PR, Fehr J, Dalmasso AP, Brigham KL, Jacob HS. Hemodialysis Leukopenia: Pulmonary vascular leukostasis resulting from complement activation by dialyzer cellophane membranes. J Clin Invest 1977; 59(January):879–88.

[42] Hakim RM, Fearon DT, Lazarus JM. Biocompatibility of dialysis membranes: Effects of chronic complement activation. Kidney Int Elsevier Masson SAS 1984; 26(2):194–200.

[43] Hakim RM. Clinical implications of hemodialysis membrane biocompatibility. Kidney Int 1993; 44(3):484–94.

[44] Ronco C, Clark WR. Haemodialysis membranes. Nat Rev Nephrol Springer US 2018; 14(6):394–410.

[45] Takeyama T, Sakai Y. Polymethylmethacrylate: One biomaterial for a series of membrane. Contrib Nephrol 1998; 125:9–24.

[46] Clark WR, Gao D, Ronco C. Membranes for dialysis: composition, structure and function. Contrib.Nephrol. 2002; 137:70–77.

[47] Cabasso I, Klein E, Smith JK. Polysulfone hollow fibers. I. Spinning and properties. J Appl Polym Sci 1976; 20(9):2377–94.

[48] Xu ZL, Chung TS, Huang Y. Effect of polyvinylpyrrolidone molecular weights on morphology, oil/water separation, mechanical and thermal properties of polyetherimide/polyvinylpyrrolidone hollow fiber membranes. J Appl Polym Sci 1999; 74(9):2220–33.

[49] Ronco C, Neri M, Lorenzin A, Garzotto F, Clark WR. Multidimensional Classification of Dialysis Membranes. Contrib Nephrol 2017; 191:115–26.

[50] Misra M. Basic mechanisms governing solute and fluid transport in hemodialysis. Hemodial Int 2008; 12(SUPPL. 2):25–28.

[51] Sam R. Hemodialysis: Diffusion and Ultrafiltration. Austin J Nephrol Hypertens 2014; 1(2):1010.

[52] Ronco C, Fabris A, Feriani M. Hemodialysis Fluid Composition. In: Jacobs C, Kjellstrand CM, Koch KM, et al., Eds. Replacement of Renal Function by Dialysis Springer, Dordrecht 1996; pp. 256–76.

[53] Azar AT, Canaud B. Hemodialysis System. In: Azar AT, Ed. Modeling and Control of Dialysis Systems Springer 2013; pp. 144–47.

[54] Ronco C, Ghezzi PM, Brendolan A, Crepaldi C, Greca G La. The haemodialysis system: Basic mechanisms of water and solute transport in extracorporeal renal replacement therapies. Nephrol Dial Transplant 1998; 13(SUPPL. 6):3–9.

[55] Kessler M, Canaud B, Pedrini LA, et al. European Best Practice Guidelines for Haemodialysis (part 1): Section II: Haemodialysis adequacy. Nephrol Dial Transplant 2002; 17(7):17–21.

[56] Vanholder R, Smet R De, Glorieux G, et al. Review on uremic toxins: Classification, concentration, and interindividual variability. Kidney Int 2003; 63(5):1934–43.

[57] Ofsthun NJ, Zydney AL. Importance of convection in artificial kidney treatment. Contrib Nephrol 1994; 108:53–70.

[58] Lorenzin A, Neri M, Clark WR, et al. Modeling of Internal Filtration in Theranova Hemodialyzers. Contrib Nephrol 2017; 191:127–41.

[59] Clark WR, Gao D, Neri M, Ronco C. Solute Transport in Hemodialysis: Advances and Limitations of Current Membrane Technology. Contrib Nephrol 2017; 191:84–99.

[60] Ross SM, Uvelli DA, Babb AL. One-Dimensional Mathematical Model of Transmembrane Diffusional and Convective Mass Transfer in a Hemodialyzer. Am Soc Mech Eng 1973; (73-WA/Bio-14):8.

[61] Villarroel F, Klein E, Holland F. Solute flux in hemodialysis and hemofiltration membranes. Trans Am Soc Artif Intern Organs 1977; 23(1):225–32.

[62] Sargent JA, Gotch FA. Principles and Biophysics of Dialysis. In: Replacement of Renal Function by Dialysis 1979; pp. 38–68.

[63] Jaffrin MY, Ding L, Laurent JM. Simultaneous Convective and Diffusive Mass Transfers in a Hemodialyser. J Biomech Eng 1990; 112:212–19.

[64] Jaffrin MY. Convective Mass Transfer in Hemodialysis. Artif Organs 1995; 19(11):1162–71.

[65] Waniewski J. Mathematical modeling of fluid and solute transport in hemodialysis and peritoneal dialysis. J Memb Sci 2006; 274(1–2):24–37.

[66] Ledebo I. Principles and practice of hemofiltration and hemodiafiltration. Artif Organs 1998; 22(1):20–25.

[67] Messer J, Mulcahy B, Fissell WH. Middle-molecule clearance in CRRT: In vitro convection, diffusion and dialyzer area. ASAIO J 2009; 55(3):224–26.

[68] Ronco C, Feriani M, Chiaramonte S, Brendolan A, Bragantini L, Conz P, Milan M, Dell'Aquila R, La Greca G. Backfiltration in clinical dialysis. Nature of the phenomenon and possible solutions. Contrib Nephrol 1990; 77:96–105.

[69] Rangel AV., Kim JC, Kaushik M, Garzotto F, Neri M, Cruz DN, Ronco C. Backfiltration: Past, Present and Future. Contrib Nephrol 2011; 175(4):35–45.

[70] Tamburini A, Renda M, Cipollina A, Micale G, Ciofalo M. Investigation of heat transfer in spacer-filled channels by experiments and direct numerical simulations. Int. J. Heat Mass Transf. 2016; 93:1190-1205.

[71] Miyagi T. Viscous Flow at Low Reynolds Numbers past an Infinite Row of Equal Circular Cylinders. J. Phys. Soc. Japan 1958.

[72] Happel J. Viscous flow relative to arrays of cylinders. AIChE J. 1959; 5:174–177.

[73] Sparrow EM, Loeffler AL. Longitudinal laminar flow between cylinders arranged in regular array. AIChE J. 1959; 5:325–330.

[74] Ishimi K, Koroyasu S, Hikita H. Mass transfer in creeping flow past periodic arrays of cylinders. J. Chem. Eng. Japan 1987; 20(5):492–498.

[75] Cancilla N, Gurreri L, Marotta G, Ciofalo M, Cipollina A, Tamburini A, Micale G. CFD prediction of shell-side flow and mass transfer in regular fiber arrays. Int. J. Heat Mass Transf. 2021; 168:120855.

[76] Magalhães HLF, Gomez RS, Leite BE, Nascimento JBS, Brito MKT, Araújo MV, Cavalcante DCM, Lima ES, Lima AGB, Farias Neto SR. Investigating the Dialysis Treatment Using Hollow Fiber Membrane: A New Approach by CFD. Membranes (Basel). 2022; 12:710.

[77] Yaqoob T, Ahsan M, Hussain A, Ahmad I. Computational Fluid Dynamics (CFD) Modeling and Simulation of Flow Regulatory Mechanism in Artificial Kidney Using Finite Element Method. Membranes (Basel). 2020; 10:139.

[78] Yaqoob T, Ahsan M, Farrukh S, Ahmad I. Design and Development of a Computational Tool for a Dialyzer by Using Computational Fluid Dynamic (CFD) Model. Membranes (Basel). 2021; 11:916.

[79] Pozzobon V, Perré P. Mass transfer in hollow fiber membrane contactor: Computational fluid dynamics determination of the shell side resistance. Sep. Purif. Technol. 2020; 241:116674.

[80] Skartsis L, Khomami B, Kardos JL. Resin flow through fiber beds during composite manufacturing processes. Part II: Numerical and experimental studies of newtonian flow through ideal and actual fiber beds. Polym Eng Sci. 1992; 32(4):231–9.

[81] Larson RE, Higdon JJL. Microscopic flow near the surface of two-dimensional porous media. Part 1. Axial flow. J. Fluid Mech. 1986; 166:449–72.

[82] Winograd Y, Toren M, Solan A. Reverse osmosis in shell and tubes. Desalination. 1974; 14:173–87.

[83] Ronco C, Scabardi M, Goldoni M, Brendolan A, Crepaldi C, La Greca G. Impact of spacing filaments external to hollow fibers on dialysate flow distribution and dialyzer performance. Int. J. Artif. Organs. 1997; 20:261–6.

[84] Li W, Liu J, He L, Liu J, Sun S, Huang Z, Liang XM, Gao D, Ding W. Simulation and experimental study on the effect of channeling flows on the transport of toxins in hemodialyzers. J. Memb. Sci. 2016; 501:123–33.

[85] Bao L, Lipscomb GG. Mass transfer in axial flows through randomly packed fiber bundles with constant wall concentration. J. Memb. Sci. 2002; 204:207–20.

[86] Bao L, Lipscomb GG. Well-developed mass transfer in axial flows through randomly packed fiber bundles with constant wall flux. Chem. Eng. Sci. 2002; 57:125–32.

[87] Sun L, Panagakos G, Lipscomb G. Effect of Packing Nonuniformity at the Fiber Bundle–Case Interface on Performance of Hollow Fiber Membrane Gas Separation Modules. Membranes (Basel). 2022; 12:1139.

[88] Cancilla N, Gurreri L, Ciofalo M, Cipollina A, Tamburini A, Micale G. Hydrodynamics and mass transfer in straight fiber bundles with non-uniform porosity. Chem. Eng. Sci. 2023; 279:118935.

[89] Cancilla N, Ciofalo M, Cipollina A, Tamburini A, Micale G. Straight fiber bundles with non-uniform porosity: Shell-side hydrodynamics and mass transfer in cross flow. Chem. Eng. Sci. 2024; 291:119947.

[90] Frank A, Lipscomb GG, Dennis M. Visualization of concentration fields in hemodialyzers by computed tomography. J. Memb. Sci. 2000; 175:239–51.

[91] Cancilla N, Ciofalo M, Cipollina A, Tamburini A, Micale G. Effects of shell-side non-ideal flow in hollow fibre membrane contactors operating in cross-flow. Proc. 41st UIT Int. Heat Transfer Conf. 2024; Naples, Italy, 19-21 June.

[92] Sangani AS, Mo G. Inclusion of lubrication forces in dynamic simulations. Phys. Fluids. 1994; 6:1653-62.

[93] Chen X, Papathanasiou TD. The transverse permeability of disordered fiber arrays: a statistical correlation in terms of the mean nearest interfiber spacing. Transp. Porous Med. 2008; 71:233-51.

[94] Matsumura Y, Jackson TL. Numerical simulation of fluid flow through random packs of cylinders using immersed boundary method. Phys. Fluids. 2014; 26:043602.

[95] Matsumura Y, Jackson TL. Numerical simulation of fluid flow through random packs of polydisperse cylinders. Phys. Fluids. 2014; 26:123303.

[96] Lemanski J, Lipscomb GG. Effect of shell-side flows on hollow-fiber membrane device performance. AIChE J. 1995; 41:2322–6.

[97] Happel J, Brenner H. Low Reynolds number hydrodynamics. Prentice-Hall, Englewood Cliffs, 1965.

[98] Skartsis L, Kardos JL, Khomami B. Resin flow through fiber beds during composite manufacturing processes. Part I: Review of newtonian flow through fiber beds. Polym. Eng. Sci. 1992; 32:221–30.

[99] Liao Z, Poh CK, Huang Z, Hardy PA, Clark WR, Gao D. A Numerical and Experimental Study of Mass Transfer in the Artificial Kidney. J. Biomech. Eng. 2003; 125:472.

[100] Eloot S, D'Asseler Y, De Bondt P, Verdonck P. Combining SPECT medical imaging and computational fluid dynamics for analyzing blood and dialysate flow in hemodialyzers. Int. J. Artif. Organs. 2005; 28:739–49.

[101] Łabęcki M, Piret JM, Bowen BD. Two-dimensional analysis of fluid flow in hollow-fibre modules. Chem. Eng. Sci. 1995; 50:3369–84.

[102] Lemanski J, Lipscomb GG. Effect of shell-side flows on the performance of hollow-fiber gas separation modules. J. Memb. Sci. 2002; 195:215–28.

[103] Ding W, He L, Zhao G, Zhang H, Shu Z, Gao D. Double porous media model for mass transfer of hemodialyzers. Int. J. Heat Mass Transf. 2004; 47:4849–55.

[104] Ding W, Li W, Sun S, Zhou X, Hardy PA, Ahmad S, Gao D. Three-Dimensional Simulation of Mass Transfer in Artificial Kidneys. Artif. Organs. 2015; 39:E79–89.

[105] Cancilla N, Gurreri L, Marotta G, Ciofalo M, Cipollina A, Tamburini A, Micale G. A porous media CFD model for the simulation of hemodialysis in hollow fiber membrane modules. J. Memb. Sci. 2022; 646:120219.

[106] Cancilla N, Gurreri L, La Rosa M, Ciofalo M, Cipollina A, Tamburini A, Micale G. Influence of bundle porosity on shell-side hydrodynamics and mass transfer in regular fiber arrays: A computational study. Int. J. Heat Mass Transf. 2023; 203:123841.

[107] Bergman T, Lavine A, Incropera F, Dewitt D. Fundamentals of Heat and Mass Transfer. 7th ed., John Wiley & Sons, 2011.

[108] Green DW, Perry RH. Perry's Chemical Engineers' Handbook. 8th ed. McGraw-Hill, editor. New York; 2008.

[109] ANSYS CFX Reference Guide Release 18.2, ANSYS Inc., Canonsburg, PA, USA, 2018.

[110] Fournier RL. Basic Transport Phenomena in Biomedical Engineering. Fourth Ed., CRC Press, Taylor & Francis Group, 2018

[111] Osuga T, Obata T, Ikehira H, Tanada S, Sasaki Y, Naito H. Dialysate pressure isobars in a hollow-fiber dialyzer determined from magnetic resonance imaging and numerical simulation of dialysate flow. Artif. Organs. 1998; 22:907–9.

[112] Cancilla N, Gurreri L, Marotta G, Ciofalo M, Cipollina A, Tamburini A, Micale G. Performance Comparison of Alternative Hollow-Fiber Modules for Hemodialysis by Means of a CFD-Based Model. Membranes (Basel). 2022; 12:118.